DYE-SENSITIZED SOLAR CELLS WITH
A SOLID HOLE CONDUCTOR

DYE-SENSITIZED SOLAR CELLS WITH A SOLID HOLE CONDUCTOR

By

LULU (LUCY) DENG, B.SC.

A Thesis

Submitted to the School of Graduate Studies

In Partial Fulfillment of the Requirements

For the Degree

Master of Applied Science

McMaster University

MASTER OF APPLIED SCIENCE (2012) McMaster University
(Department of Materials Science and Engineering) Hamilton, Ontario

TITLE: Dye-sensitized Solar Cells with a Solid Hole Conductor

AUTHOR: Lulu (Lucy) Deng, B.Sc. (Sun Yat-sen University)

SUPERVISOR: Professor Gu Xu

NUMBER OF PAGES: x, 81

Abstract

Dye-sensitized Solar Cells (DSSCs) with liquid electrolyte lack long term stability because of volatility of the electrolyte and assembly problems. Replacement of the volatile liquid-state electrolyte with solid-state hole conductor thus becomes necessary. A small molecule based hole conductor, Copper Phthalocyanine (CuPc), is proposed here to replace the liquid electrolyte, for its intrinsic thermal and chemical stabilities. However, a lower short circuit current was found in the CuPc solid state device from I-V curve, which is closely related to the inefficient hole transport in the CuPc thin film. Therefore, Two-Dimensional Grazing Incidence X-ray Diffraction (2D GIXRD) is utilized to study the phase and texture of CuPc thin film. It is found that the CuPc thin film has an average crystallite size of about 24 nm. In addition, crystallites in the thin film had two preferred orientations, $(20\bar{1})$ and (001), with $(20\bar{1})$ dominating. The crystallites in both orientations have a preferential ordering along the substrate normal, and are randomly oriented in-plane. Besides, the film has a cystallinity of greater than 80%, which is good for hole conducting. However, the β-phase formation lowers the overall hole conductivity. The hole conductivity of β-phase CuPc is two orders of magnitude smaller than that of α-phase CuPc, due to a less overlap in the π-π stacking. As a result, the low hole conductivity of β-phase CuPc is the reason that leads to an inefficient hole transport and reduces the short-circuit current of the solid-state DSSC. Therefore, future work will be necessary to isolate α-phase CuPc, in order to be successfully applied into the solid-state DSSCs.

Acknowledgements

I am heartily thankful to my supervisor, Dr. Gu Xu, for his patient guidance, inspiring encouragement and invaluable ideas throughout my master study. His pure unselfish and honest passions to science as well as the critical and logical problem solving strategies deeply influenced me.

I would like to thank Dr. Jim F. Britten, for his useful discussion and professional support in my X-ray diffraction experiment. I am also deeply grateful to Jim Garrett, for his instant assistance and instructive suggestion.

My group members, Cindy Xinxin Zhao, Matthew Yiqun Ma, Kewei Wang and Han Yan have always assisted me. I would like to thank them for their great company and helpful advice with this project.

Members of my family and many more than I can include here, have loved me far beyond what I can ever return. My parents, Weidong Deng and Meixia Zhou always support me throughout my study overseas. I wish to give my most sincere gratitude for their guidance and confidence to help me overcome the difficulties during my master study. Special thank is given to my boyfriend Chang Liu for his continuous trust and constructive discussion.

The great support from Department of Materials Science and Engineering at McMaster University, as well as Natural Science and Engineering Research Council of Canada (NSERC) is greatly appreciated.

Table of Contents

List of Figures

List of Tables

Chapter 1 Introduction

1.1 Solar Cell Types

It has become a common sense to everyone that we are now living in a world, in which traditional fossil energy is being consumed at an unprecedented rate. A serious problem, namely global warming, has originated from the use of fossil fuel. As a solution, renewable energy sources serve as a key ingredient for the development of a globally sustainable society. Among the existing renewable energy sources, solar energy is one of the most promising.

Solar Cells are opto-electronic devices that convert solar energy directly to electrical energy by photovoltaic effect - the creation of a voltage or an electric current in an illuminated junction [1]. There are mainly three types of solar cells according to the materials they employ: inorganic, organic and hybrid, as shown in Figure 1.

Inorganic solar cells, such as silicon-based and III-V compounds based, are dominating the solar cell market with the typical power conversion efficiency of up to 20 % [2][3]. A typical inorganic solar cell is composed of two metal electrodes, p/n semiconductor junction and an optional anti-reflection coating, as shown in Figure 2.

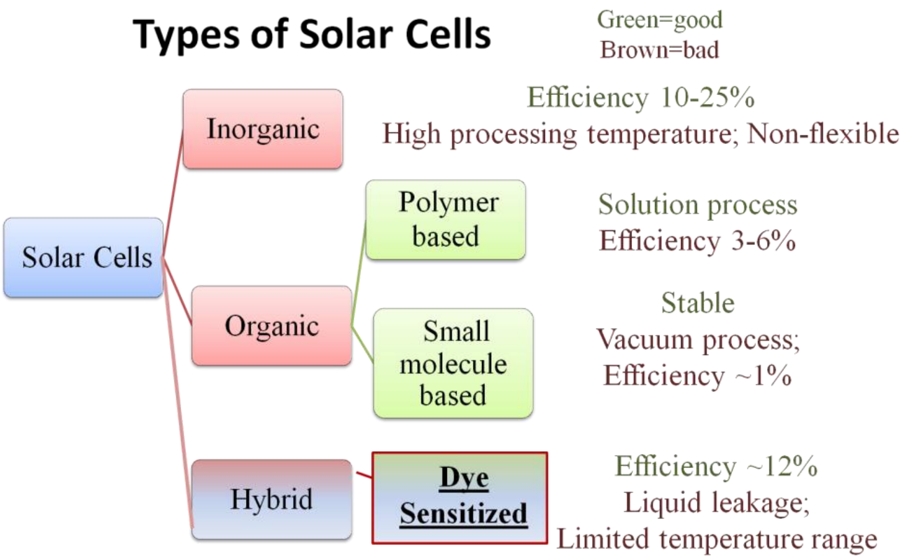

Figure 1: Types of solar cells.

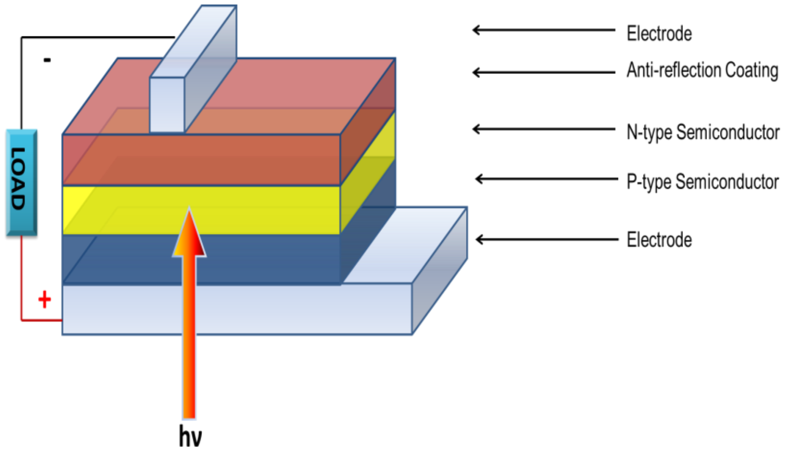

Figure 2: The structure of inorganic solar cells [4].

Although inorganic solar cells govern the solar cell market, the manufacturing processes often involve costly, high vacuum, and numerous lithographic steps, resulting in a high production cost and high energy consumption [5] [6].

Still in their infancy, organic solar cells are divided into two categories, polymer based and small molecule based. Polymer based organic solar cells are flexible and easy to fabricate, while small molecule based organic solar cells are intrinsically stable [7]. Organic solar cells have relatively low power conversion efficiency [3] and have not yet entered into the commercial market.

The third type of solar cell is hybrid solar cell. One representative is Dye-Sensitized Solar Cell (DSSC). This is the focus of the present thesis. There are two categories of DSSCs, with liquid electrolyte or solid hole conductors [8] [9] as redox mediator. The power conversion efficiency of DSSCs with liquid electrolyte is higher than that of DSSCs with solid-state hole conductors, the latter is comparable to the power conversion efficiency of organic solar cells (~ 4 % [3] [9]). Currently, the highest power conversion efficiency of DSSCs with liquid electrolyte is 12.3 % [10].

The typical dye-sensitized solar cell has sandwich configuration, as shown in Figure 3. It includes working electrode, dye, redox mediator and counter electrode.

The typical structure of a DSSC with liquid electrolyte is shown in Figure 3. Light comes into the device from the left side, passing through a piece of conducting glass which is used to collect electrons, a compact layer of TiO_2 preventing short circuit current, and finally reaching the nanoporous working electrode of TiO_2. There is a monolayer of dye molecules attached to the surface of the TiO_2 nanoporous working electrode, which is employed to convert solar energy into electricity. On the right side, there is a counter electrode, consisting of a thin layer of catalyst and another piece of conducting glass. An electrolyte lies between the two electrodes, which shuttles the electrons between the working electrode and counter electrode, and thus completes the circuit.

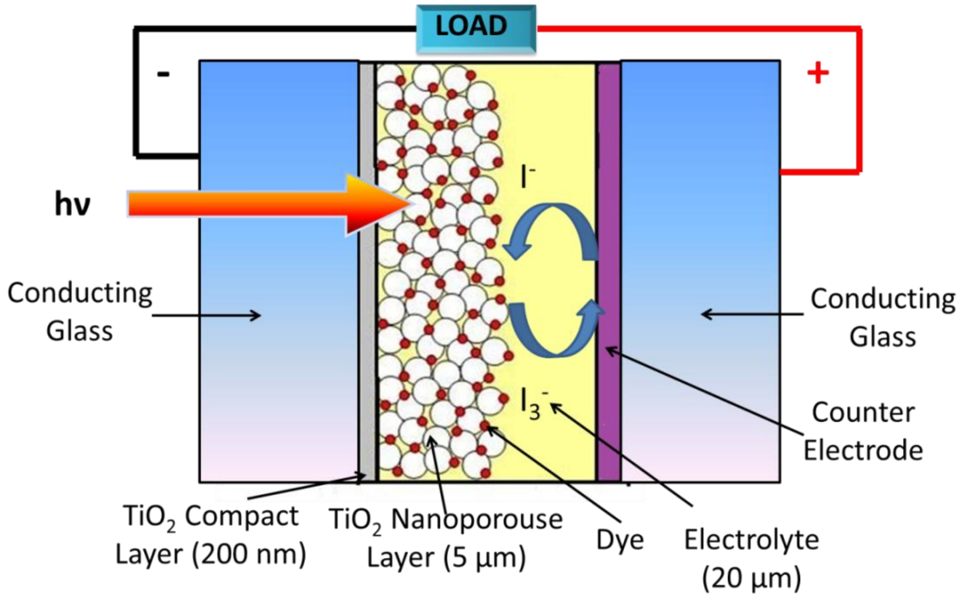

Figure 3: The structure of dye-sensitized solar cells (DSSCs).

In general, the materials of the working electrode are metal oxides with wide band gaps. Titanium dioxide (TiO_2), zinc oxide (ZnO) and tin oxide (SnO_2), all with a band gap around 3.2 eV, have been widely used in dye-sensitized solar cells [11]. The nanoparticles of these semiconductor metal oxides form a semitransparent and nanoporous working electrode (see Section 1.2).

The monolayer of dye molecules on the surface of TiO_2 nanoporous working electrode is responsible for electron harvest. The ruthenium based complex dyes, such as di-tetrabutylammonium cis-bis (isothiocyanato)bis (2,2'-bipyridyl- 4,4'-dicarboxylato) ruthenium(II) (N719, also known as black dye) [12] and cis- di(thiocyanato) bis(2,2'-bipyridyl -4-4'-dicarboxylate) ruthenium(II) (N3) [13] have been widely used in DSSCs. The power conversion efficiency of DSSCs with N719 dye or N3 dye is the highest (~11 %). Figure 4 shows the molecular structure of N719 and N3. An efficient electron injection from the excited dye to TiO_2 requires that the thickness of dye molecules is around 1 nm, thus light absorption by the monolayer of dye molecules is limited. As a result, more efforts have been made to synthesize new dyes with high photon absorption coefficients.

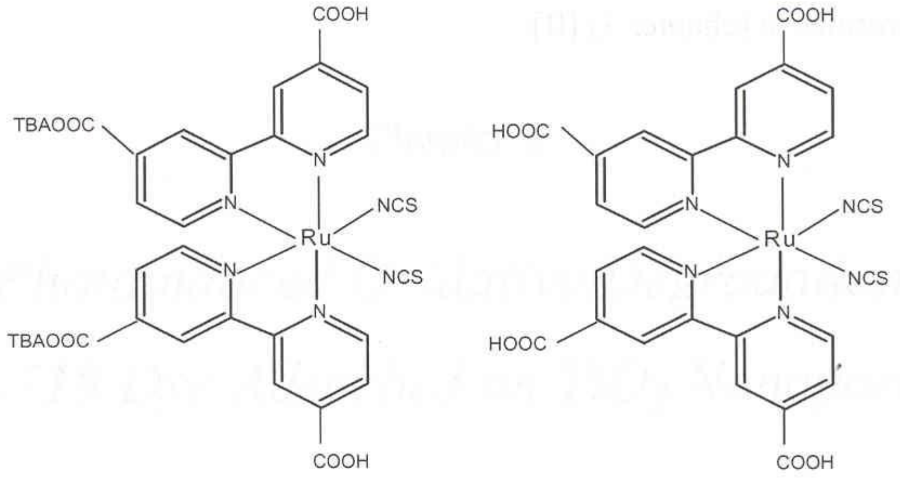

N719 N3

Figure 4: Molecular structures of N719 and N3. [11]

For the redox mediators, iodide/triiodide (I^-/I_3^-) redox couple has been a preferred choice due to its suitable redox potential [14]. Other redox couples, for example cobalt-based systems [10], Br^-/Br_3^- [15], $SCN^-/(SCN)_3^-$ and $SeCN^-/(SeCN)_3^-$ [16] have been attractive, because their redox potentials are closer to the ground state of the dyes, which provide a higher output voltage.

The counter electrode is used to catalyze the regeneration of I^-. The widely used material for the construction of the counter electrode is platinum. An efficient regeneration of I^- increases the diffusion rate of I^- and finally increase the reduction rate of the oxidized dye.

1.2 Operation Principle of Dye-sensitized Solar Cells

In a dye-sensitized solar cell, the procedure of light-to-electricity conversion includes five steps [17]， which are described by the energy band diagram [14], as shown in Figure 5.

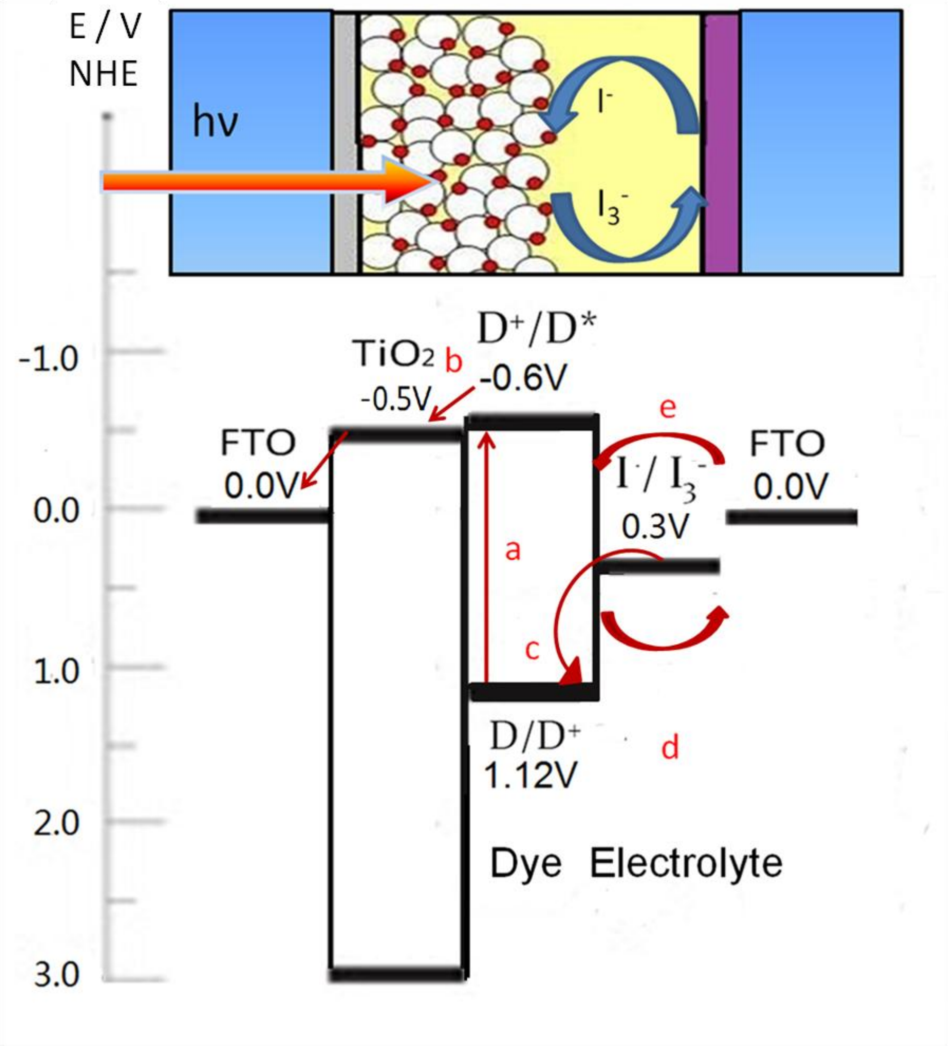

Figure 5: Band diagram of a DSSC with liquid electrolyte.

In Figure 5, the potentials are shown for a DSSC based on N719 dye, TiO_2, and I^-/I_3^- redox couple. The substrate is fluorine doped tin oxide (FTO, F: SnO_2)

conducting glass. The five steps of light-to-electricity conversion are thus described as follows

a. $D+hv \rightarrow D^*$;

b. $D^* \rightarrow D^+ + e_{CB}$

c. $D^+ + I^- \rightarrow I_3^- + D$

d. I_3^- diffusing to the counter electrode ;

e. $I_3^- \rightarrow I^-$, diffusing to dye molecules

Light comes into the dye-sensitized solar cell, arriving at the TiO_2 nanoporous working electrode. After absorbing photons, the dye molecules adsorbed on the surface of the nanoporous working electrode will be promoted from their ground state (D) to the excited state (D*), as shown in the first step (a). The excited dye molecules will then inject electrons (e_{CB}) to the conduction band of the TiO_2 working electrode, becoming oxidized (D^+) (step (b)). The electrons (e_{CB}), transported through the compact layer of TiO_2 and the conducting electrode, will finally go into the external circuit and contribute to the electricity output. To complete the internal circuit, the oxidized dye molecules (D^+) will be reduced to the ground state (D) by receiving the electrons from iodide (I^-) in the electrolyte, as depicted in the third step (c). After reducing the oxidized dye, I^- will be oxidized to triiodide (I_3^-) and diffuse to the counter electrode caused by the concentration gradient (step (d)). Finally, I_3^- will be reduced to I^- by receiving the electrons from the external circuit, catalyzed by platinum catalyst on the counter electrode. I^- will diffuse back to the solid-liquid interface, and thus form a loop between the working electrode and counter electrode (step (e)) [18].

In Figure 5, the electrochemical potentials are all compared to normal hydrogen reference electrode (NHE) [14]. The potentials determine whether the reaction can happen spontaneously. According to thermodynamics, if the change of Gibbs free energy ΔG is negative (Equation 1.1), the reaction is spontaneous [19].

$$\Delta G = -nEF \tag{1.1}$$

where 'n' represents the number of electrons transporting in the system; 'F' is the Faraday Constant (F= 96,485.3415 C/ mol); 'E' is the redox potential taking NHE as a reference, resulting from Nernst equation.

The following calculation shows the reason why it is the iodide (I^-) to reduce the oxidized dye instead of (I_3^-).

$$\frac{1}{2}\mathbf{I}_3^- + \mathbf{e}^- = \frac{3}{2}\mathbf{I}^- \qquad \text{E=0.3 V} \tag{1.2}$$

$$\mathbf{D}^+ + \mathbf{e}^- = \mathbf{D} \qquad \text{E=1.12 V} \tag{1.3}$$

Subtracting (1.3) by (1.2) gives

$$\mathbf{D}^+ - \frac{1}{2}\mathbf{I}_3^- = \mathbf{D} - \frac{3}{2}\mathbf{I}^-, \quad \therefore \mathbf{D}^+ + \frac{3}{2}\mathbf{I}^- = \mathbf{D} + \frac{1}{2}\mathbf{I}_3^-, \text{ E=0.82 V} \tag{1.4}$$

Thus, $\Delta G = -nEF$ is negative, showing that iodide (I^-) will spontaneously reduce the oxidized dye.

A key component in dye-sensitized solar cell is the nanoporous working electrode prepared by semiconductor metal oxides nanoparticles, which largely enhances the surface area of the working electrode. This allows more dye molecules to be adsorbed, and thus improving the light absorption efficiency (the ratio of the number of electrons, converted from photon absorption, over the number of input photons, IPCE [11]). In the late 1960's, the first dye-sensitized photogalvanic cell was fabricated by Gerischer's group, using ZnO single crystal as the working electrode. The device produced a power conversion efficiency of less than 0.5 %. The smooth working electrode limited the dye loading, leading to an insufficient light absorption [20]***.*** Since the mid 1980's, the record of DSSC power conversion efficiency has been kept by Gratzel's group in Switzerland. In 1991, this group fabricated a nanocrystalline dye-sensitized solar cell with power conversion efficiency of approximately 7 %, which was a breakthrough in the development of dye-sensitized solar cells. The novelty of this device is the employment of a nanoporous working electrode, which effectively increases the surface area by about 700 times, allowing for a larger amount of dye molecules adsorbed on the surface, and thus enhances the power conversion efficiency [17].

1.3 Kinetics of Dye-sensitized Solar Cells

An appropriate kinetic competition at the interfaces distinguishes DSSC from inorganic and organic solar cells. In inorganic and organic solar cells, there is no kinetics competition at the interface. A photo generated exciton (electron-hole pair) diffuses to the interface of a p/n junction (consisting of p-type and n-type semiconductors) and is then separated by the built-in electric field [21]. The direction of electron transport depends on the direction of the internal electric field. In a DSSC, the transport direction of electron is determined by the result of the kinetic competition at different interfaces [17].

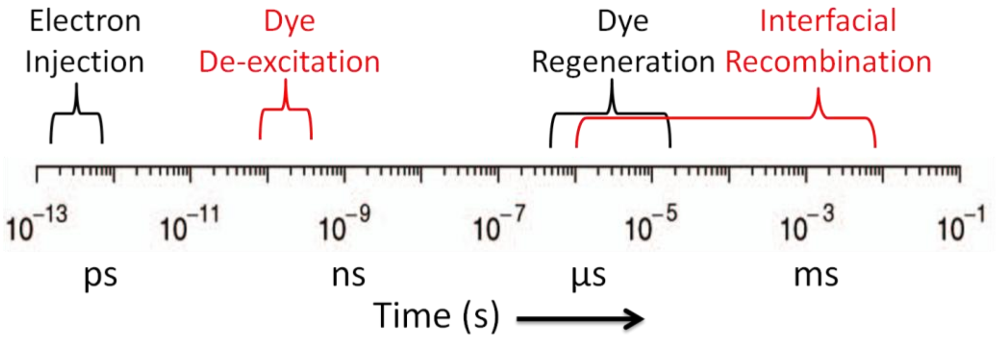

Figure 6: The kinetics of key processes (electron injection, dye de-excitation, dye regeneration and interfacial recombination) in DSSCs [9].

Figure 6 shows the time scale of the key processes in DSSC. Among all the processes, electron injection from the excited dye to the conduction band of the working electrode is the fastest, and is between 100 femotoseconds and 100 picoseconds [22]. This is followed by the self-de-excitation process of the excited dye, which is in nanosecond (ns) scale [22]. The reduction of oxidized dye takes place in a few micron seconds (µs), competing with the interfacial recombination, for instance, between electrons in TiO_2 and the oxidized dye or between electrons in TiO_2 and the redox electrolyte [23] [24]. The time scales vary in different experimental conditions. However, it is required that the oxidized dye regeneration should occur significantly faster than the interfacial recombination for an efficient DSSC, to lower the internal loss.

1.4 I-V Characteristics

The power conversion efficiency and other basic photovoltaic parameters (*e.g.* series resistance, parallel resistance, fill factor) of dye-sensitized solar cells can be obtained from the current density – voltage

(I-V) characteristics, as shown in Figure 7.

Under illumination, the open-circuit voltage (V_{oc}) is achieved when there is no photo-generated current ($J= 0$). It is determined by the difference between the redox potential of the electrolyte and the bottom of the conduction band of working electrode materials. The short-circuit current (J_{sc}) is obtained under the short-circuit condition ($V= 0$). It largely depends on the photon generated electrons and the interfacial recombination of the electrons and holes. The series resistance (R_s) of the DSSC generally involves bulk resistance and the interfacial resistance. Its reciprocal is estimated by the slope of the I-V curve at $V= V_{oc}$. The parallel resistance (R_p) represents the internal recombination, whose reciprocal is estimated by the slope of the I-V curve at $J= J_{sc}$. The fourth quadrant of the I-V plot is the operation region for dye-sensitized solar cells (DSSCs), where DSSCs generates power (power= |current × voltage|). At a certain point, the product between current and voltage and hence the power output arrives at maximum, which is named as the maximum power point (MPP).

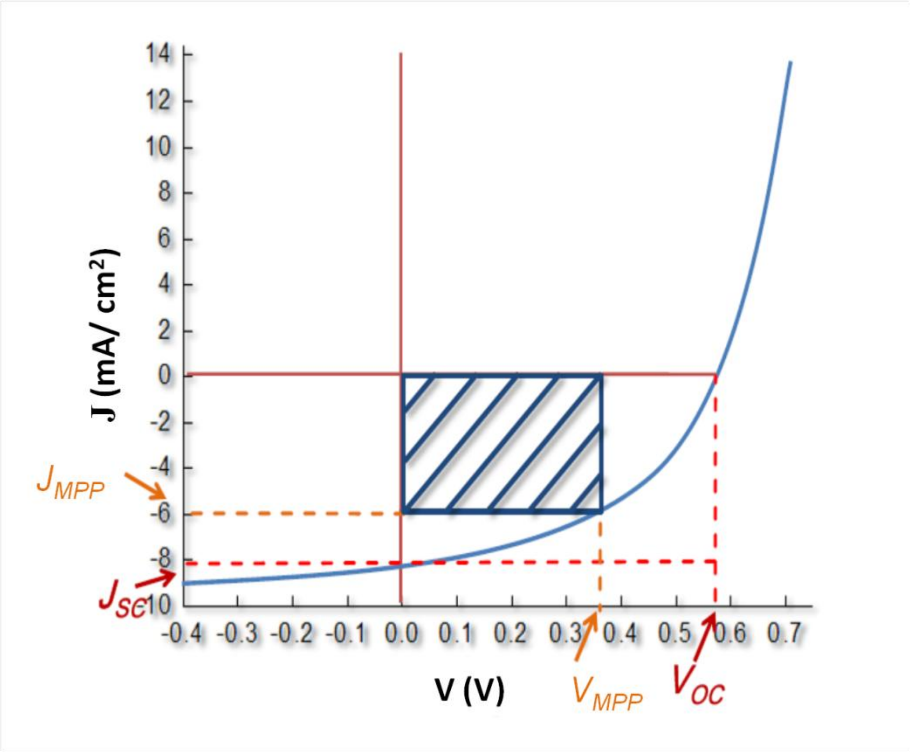

Figure 7: The I-V characteristics of a DSSC [4]

To determine the power conversion efficiency (η) of a dye-sensitized solar cell, the maximum output power (P_{output}) should be compared with the input photon power (incident light intensity, P_{input}), as shown in Equation (1.5).

$$\eta = \frac{P_{output}}{P_{input}} = \frac{J_{sc}V_{oc}FF}{P_{input}} \tag{1.5}$$

Another important parameter called the fill factor (FF), depicting the squareness of the I-V plot, is calculated by Equation (1.6), the maximum obtainable power over the product of the V_{oc} and J_{sc} [25].

$$\mathrm{FF} = \frac{J_{MPP}V_{MPP}}{J_{sc}V_{oc}} \tag{1.6}$$

The shape of the I-V plot can be fitted with a basic diode equivalent circuit model of solar cells [26] (Figure 8). To achieve a larger output voltage and current, the series resistance is expected to be the smaller the better, while the parallel resistance is the larger the better. Correspondingly, in the I-V plot (Figure 7), the slope at V= V_{oc} should be steep and at J= J_{sc} be flat.

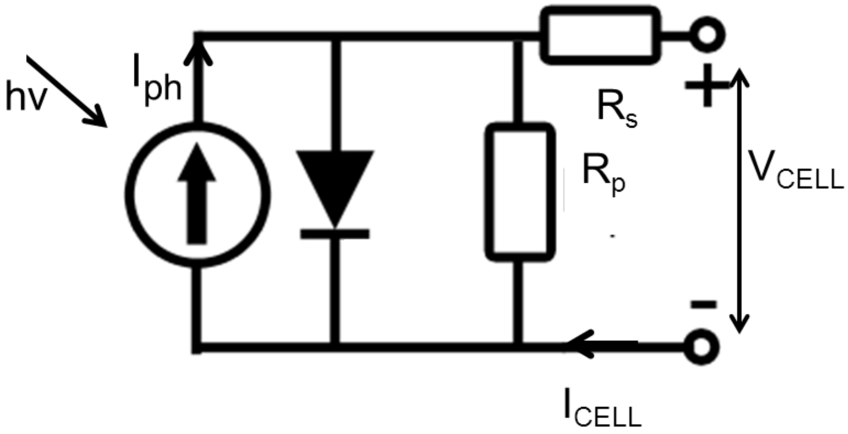

Figure 8: Basic diode equivalent circuit of a solar cell. I_{ph} is the photocurrent density modeled as a current source. R_s and R_p represent the series resistance and parallel resistance, respectively.

1.5 Applications of Dye-sensitized Solar Cells

Due to the advantages of light weight, low cost and flexibility, DSSCs are being developed into consumer applications. For example, DSSCs are integrated into bags, portable electronic devices, serving as charging stations, as depicted in Figure 9a [27] and b [28]. Samsung has manufactured dye-sensitized solar cell battery to support mobile charging [28], with a cost between one third and one fifth of the existing silicon based photovoltaic products.

The performance of dye-sensitized solar cells is less sensitive to the illumination conditions compared to the inorganic solar cells. The rough surface of the working electrode can absorb incident light from different directions [31]. Therefore, they are able to provide electricity to low-power electrical equipments even under low illumination conditions，as shown in Figure 9c.

Moreover, building-Integrated photovoltaics, which employs photovoltaic devices in building structures such as windows, skylights, roofs and walls to provide electric power for the building and save electric energy, can be benefited from dye-sensitized solar cells, because of their flexibility, easy installation and better performance in low and indirect illumination. Figure 9d [30] shows an example that the DSSC attached windows can be integrated into buildings.

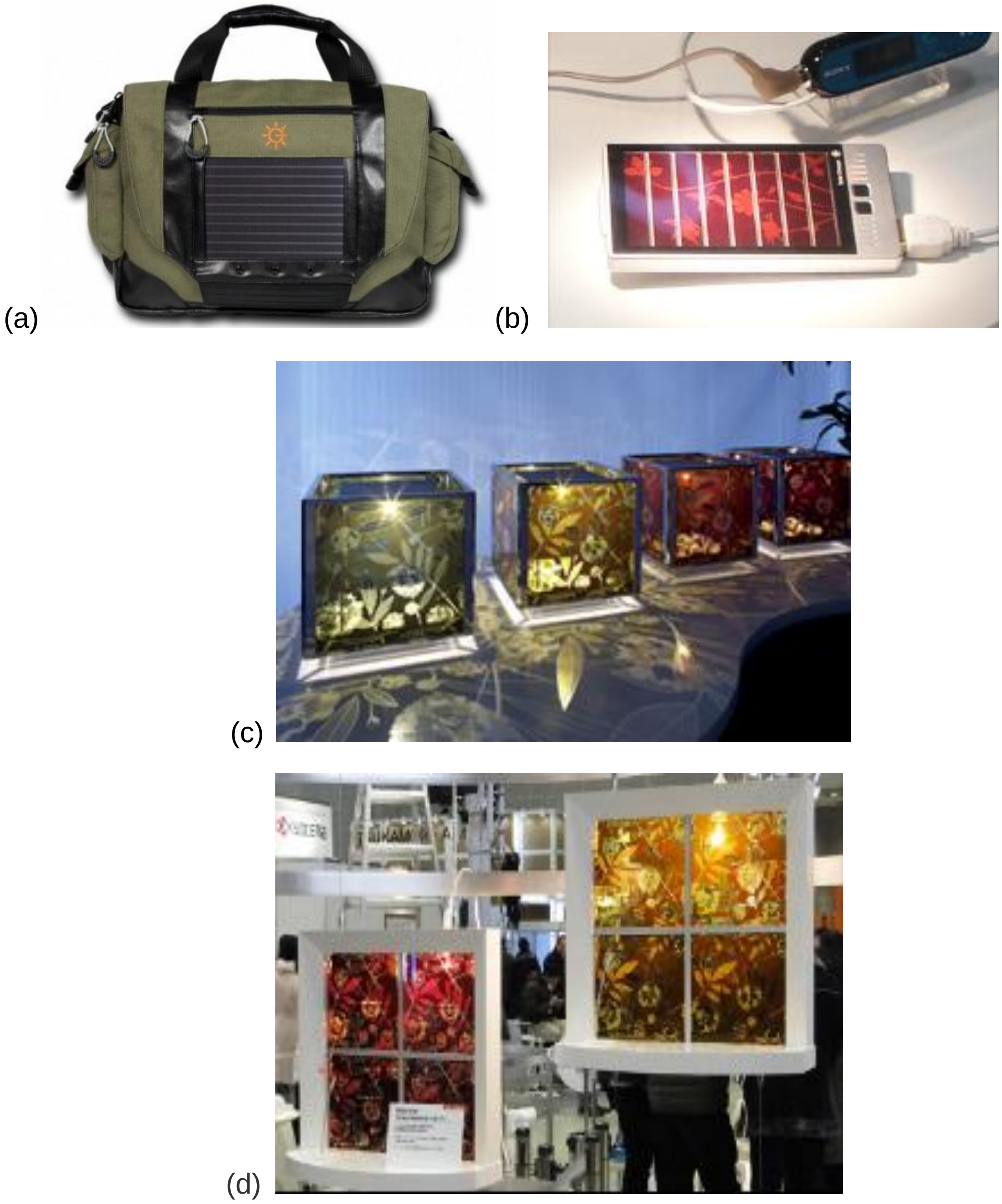

Figure 9: DSSC integrated into (a) bag [27] and (b) portable electronic device [28], serving as chargers, manufactured by Samsung; (c) DSSC powered lamps produced by SONY [29]; (d) DSSC attached windows [30].

1.6 Research Objectives

Since dye-sensitized solar cells (DSSCs) with liquid electrolyte lack long term stability, because of the volatility of the electrolyte and assembly problems, the replacement of the volatile liquid-state electrolyte with solid-state hole conductor becomes necessary.

As a primary goal, a small molecule based hole conductor, copper phthalocyanine (CuPc), is proposed here to replace the liquid electrolyte, for its intrinsic thermal and chemical stabilities. However, the solid-state DSSC with CuPc shows a low short-circuit current, which is closely related to the inefficient hole transport in the CuPc thin film, therefore, the major objective of the thesis is to explore the phase and texture of CuPc thin film by 2D grazing incidence X-ray diffraction, as well as to further explain the inefficient hole transport and low short-circuit current found in the solid state DSSC with CuPc.

1.7 Thesis Overview

The thesis consists of six chapters. Chapter 1 provides the introduction of dye-sensitized solar cells (DSSCs), including the solar cells classification, typical structure of DSSCs, operation principle, potential applications and research objectives. Chapter 2 involves literature review, including the main challenges of dye-sensitized solar cells and previous works. Chapter 3 introduces the experimental procedure and instrumentation. Chapter 4 covers results and discussion. It includes the duplication of DSSC with liquid electrolyte, the results by replacing the electrolyte with solid hole conductor copper phthalocyanine (CuPc), and the exploration of the phase and texture of CuPc thin film by 2D grazing incidence X-ray diffraction, which has been published in a refereed journal of *Crystals (*2011*,1)*. Chapter 5 is the conclusions and Chapter 6 the future work.

Chapter 2 Literature Review

2.1 Remaining Challenges for Dye-sensitized Solar Cells

Although dye-sensitized solar cells (DSSCs) have the advantages of low cost, flexibility, transparency and easy fabrication, they are not yet commercially available in a large scale. Remaining challenges for DSSCs are listed in detail as follows.

2.1.1 Low Current Density

The output current density of dye-sensitized solar cells (short-circuit current ~18 mA/cm^2 obtained from the state-of-the-art DSSC [32]) is in general much lower than that of the inorganic solar cells, especially the silicon based. A key component in DSSCs' design is the nanoporous working electrode with a pore size of ~20 nm and a porosity of around 50 % [9]. Although it increases dye loading, light absorption and improves the interpenetration of liquid electrolyte, the non-uniform interface creates a lot of trapping points, which quench the electrons and lead to a decrease of the output current. These trapping points are usually the boundaries of the nanoparticles and defects [34]. In a DSSC with I^-/I_3^- redox couple under ideal circumstances, interfacial recombination happens in microseconds, slower than the electron transport within nanoporous layer [35]. However in reality, defects in the nanoporous layer slow down the speed of electron transport, which results in internal losses.

The losses will take place at the TiO_2 / liquid electrolyte interfaces, where electrons recombine with either the oxidized dye or I_3^- before contributing to the external output [35], as shown in Figure 10.

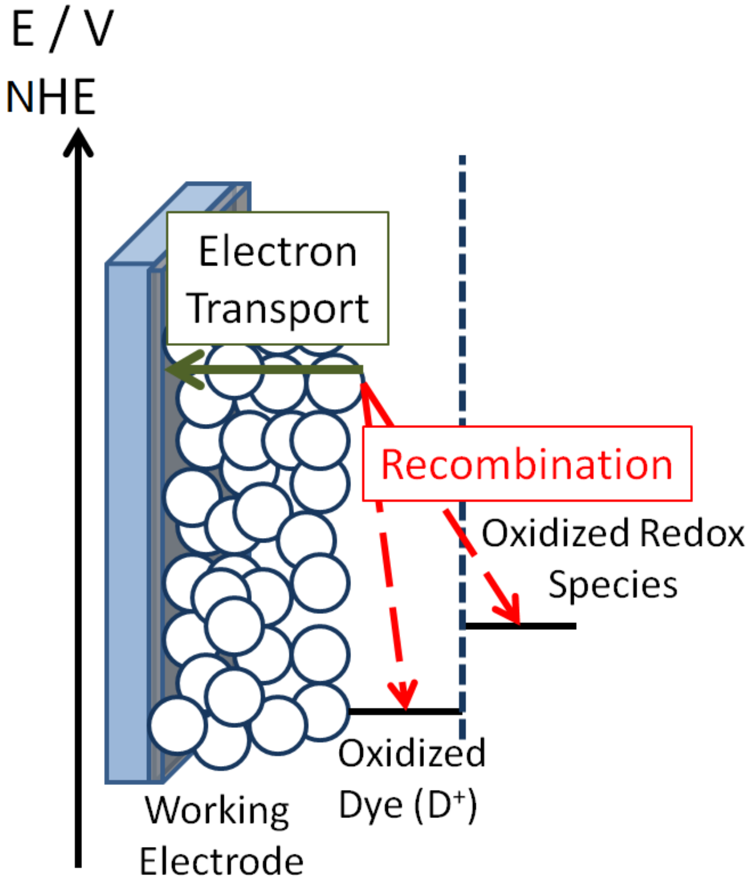

Figure 10: Illustration of interfacial recombination in a DSSC.

Another factor leading to low current density is the limited light absorption. In typical DSSCs, the high surface area of the nanoporous working electrode increases the light absorption by around 700 times compared with the smooth surface of the single crystalline electrodes, which is not enough [17]. In order to further improve the light absorption, dyes with higher photon absorption coefficient are synthesized. Here, photon absorption coefficient describes the capability of a chemical species to absorb light at a specific wavelength [36]. There are two types of dyes used in DSSCs: metal-based dyes and metal-free organic dyes. Ruthenium based dyes, as a representative of the former category, has a lower photon absorption coefficient (for example, N719: 14.0 × 10^3 M^{-1} cm^{-1}). Organic dyes have higher photon absorption coefficient (~18.2× 10^3 M^{-1} cm^{-1}) [36], due to a narrower band gap responding to a broader spectrum [37]. It should be noted that the definition of band gap is different for metal based dyes from organic dyes. For metal based dyes, band gap refers to the difference between the excitation energy and the ground energy. For organic dyes, it represents the difference between the highest occupied molecular orbital (HOMO) and the lowest unoccupied molecular orbital (LUMO) [25]. However, the absorption band gap cannot be too small, which would result in insufficient driving energy for election injection to the conduction band of the working electrode, and/or the dye regeneration by redox mediator. It remains a challenge to find an appropriate organic dye that fits the requirements，balancing the photo voltage and photo current at the same time.

2.1.2 Low Open-circuit Voltage

In principle, the open-circuit voltage depends on the difference between the conduction band and the redox potential of the electrolyte species. In practice, open-circuit voltage is inevitably influenced by the trapping states on the semiconductor metal oxide. To keep an efficient regeneration of oxidized dye, the redox potential of the redox mediator needs to be lower than the ground state of dye. The most popular electrolyte in the system is iodide/triiodide (I^-/I_3^-). The advantage of this redox couple is the low recombination reaction rate from the working electrode to triiodide (I_3^-) [14], which provides an efficient electron collection on the photo anode (working electrode). However, its relatively low redox potential limits the open-circuit voltage [18]. Figure 11 illustrates that the redox potential difference between dye N719 (1.12 V *vs.* NHE) and I^-/I_3^- (0.3 V *vs.* NHE) has exceeded 600 mV. If the absorbed photon energy is 2 eV, the dye reduction energy by I^-/I_3^- redox couple will consume more than 30 % of it, resulting in a reduced output energy of electricity. The open-circuit voltage can be improved by using redox couples of more positive redox potentials, for example, ferrocenium/ferrocene (Fc^+/Fc) (0.62 V) shown in Figure 11.

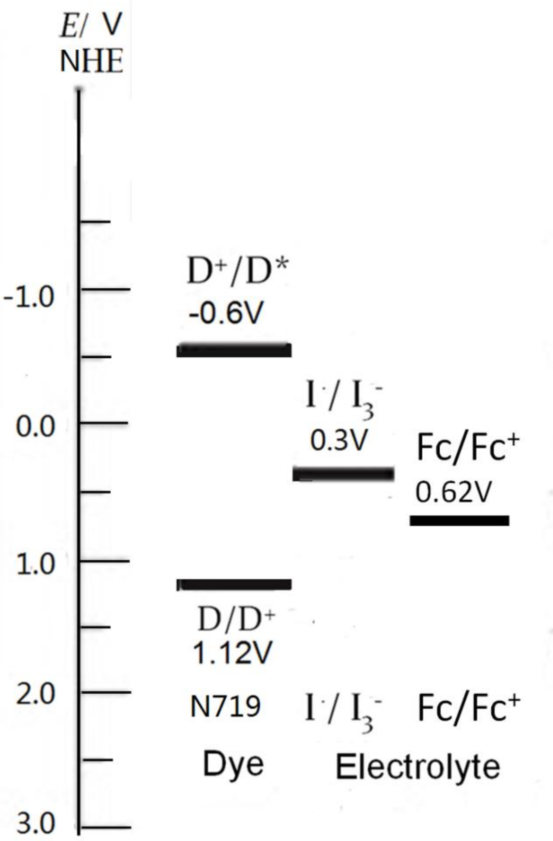

Figure 11: Energy level of DSSC components, approximate redox potentials and band energies of the different components. Data for N719, I^-/I_3^- and Fc/Fc^+ *versus* normal hydrogen electrode (NHE) [14]

Based on the above facts, new electrolytes with a larger positive redox potential is under active investigation. Examples include cobalt polypyridine redox mediator [38], copper complexes [39], ferrocenium/ferrocene (Fc^+/Fc) [40] and so on. Among them, non-corrosive Fc^+/Fc shows a high potential to increase the open-circuit voltage by decreasing the dye regeneration driving force, and to quickly reduce the oxidized dye. However, the recombination rate between the electrons in TiO_2 and Fc^+ is high, therefore the photo current decreases [41].

To summarize, it remains a challenge to find an alternative of electrolyte with less dye regeneration driving force, but without compromising the efficient electron transport at the solid / liquid interface.

2.1.3 Stability Issues

Besides power conversion efficiency, stability serves as a key factor to commercialization. Two factors contribute to the stability of a dye-sensitized solar cell (DSSC). One is physical stability, and the other chemical stability.

In order to improve physical stability, progresses have been made in the sealing and assembling procedures. In the 1991 paper by Gratzel's group, the electrolyte was injected into the nanoporous layer by capillary force without sophisticated sealing [17]. Surlyn films (DuPont), a kind of hot melt gaskets, was later introduced into the device assembly, helping to prevent the leakage or evaporation of the volatile electrolyte, as well as to control the thickness between the working electrode and the counter electrode [32]. The purpose of using volatile electrolytes is to form a good contact and a complete interpenetration at the interface of the nanoporous working electrode and liquid electrolyte, as well as to facilitate the diffusion of the redox couple. Therefore, the electrolyte has to have low viscosity. A solvent with low viscosity is usually accompanied by a low boiling point at normal pressure (*i.e.*, volatile). Take the commonly used solvent acetonitrile as an example. The viscosity of acetonitrile is 0.34 mPa·s, much lower than that of water (0.89 mPa·s). On the other hand, the boiling point of acetonitrile at ambient pressure is 81°C, compared to 100°C for water [11]. As a result, to prepare the electrolyte, ~15 volume percent of valeronitrile is added, which has a boiling point is 139°C. The usage of electrolyte with higher boiling point helps to improve the physical stability of the DSSC, since it reduces the evaporation rate.

More efforts have been made to analyze the chemical stability of DSSCs. The commonly used redox couple I^-/I_3^- itself is unstable under UV light, since iodine, a necessary component in the formation of the redox couple, will be oxidized under UV radiation, which blocks the I_3^- reduction at the counter electrode. [42].

When the electrolyte is injected into the DSSC system, more factors affect the stability of the device, which include thermal and electrochemical degradation. Thermal degradation usually happens above 80°C, due to the volatility of the electrolyte solution [43]. Electrochemical degradation happens when an ionic ligand of the functional dye is replaced by another ion (I_3^-), usually under elevated temperature and light exposure. Hagfeldt’s group found that the thiocyanate ion ligand (NCS^-) in N719 dye molecules subjects to both thermal and electrochemical degradation under light illumination at a high temperature of about 135°C, which will be replaced by triiodide (I_3^-) in the electrolyte [44]. For this reason, the additive 4-tert-butylpyridine (4TBP) is usually added to the I^-/I_3^- electrolyte, slowing down the exchange between I_3^-

and NCS^- [45], which can be described by the following reactions.

$$(dcbpy)_2Ru(SCN)_2^{2-} + 2I_3^- \rightarrow (dcbpy)_2RuI_2^{2-} + 2I_2SCN^- \qquad (2.1)$$

$$(4TBP) + I_3^- \rightarrow (4TBP)I_2 + I^- \qquad (2.2)$$

$$(4TBP) + I_3^- \rightarrow (4TBP)I^+ + 2I^- \qquad (2.3)$$

Equation (2.1) shows the exchange between the SCN^- ion ligand and I_3^-. Equation (2.2) & (2.3) show the reactions between the additive 4TBP and I_3^-, which would suppress the loss of SCN^- ion ligand.

Moreover, it has been reported that the N719 loading on TiO_2 surface relies on the thiocyanate ion ligand (SCN^-). Once the exchange between I_3^- and NCS^- occurs, dye N719 will no longer be attached to the TiO_2 surface, due to the loss of SCN^-, and thus decreases the light absorption and the short-circuit current [46].

Another factor influencing negatively the durability is the residual water in the electrolyte. During the preparation process of the electrolyte, the solvent cannot be 100 % anhydrous. According to the work of Lu *et al*. [47], the presence of water in the electrolyte will decrease the resistance at the TiO_2 / electrolyte interface, resulting in a faster recombination between the injected electrons in TiO_2 and the I_3^- in the electrolyte, and leading to a decrease of the short-circuit current [47].

Besides the above factors that would reduce the device life-time, the corrosive effect of the redox couple I^-/I_3^- to the counter electrode made by silver involved in the module manufacturing is also found to hamper the device durability [42]. As a result, new electrolytes with high corrosive resistance are required, as mentioned in section 2.1.2.

2.2 Previous Work to Increase the Power Conversion Efficiency

More efforts have been made to increase the power conversion efficiency, among which the synthesis of new nanostructure of both working and counter electrode takes up a large portion. More uniform nanostructure of TiO_2, *e.g.* TiO_2 nanotube [48] has been developed, in order to increase the surface area, allowing more dye loading without big aggregation, as well as to enhance electrolyte percolation and diffusion in the nanostructure. In 2006, Grimes's group synthesized highly-ordered TiO_2 nanotubes on FTO conducting glass to fabricate a DSSC with a power conversion efficiency of 2.9 %. The TiO_2 nanotubes have a pore diameter of 46 nm, a wall thickness of 17 nm, and a length of 360 nm. A higher power conversion efficiency was predicted by increasing the length of TiO_2 nanotube [48].

In addition, a more uniform pore size in the ordered nanostructure plays a vital role in enabling a complete interpenetration of the hole conductors during the device fabrication, helping to reduce the interface recombination. On top of that, surface modification of TiO_2 has been studied. For example, a thin layer of $SrTiO_3$ deposited on the surface of TiO_2 formed a core-shell structure. It helped the TiO_2 conduction band to shift upward, closer to the excited state of dye, which enlarges the open-circuit voltage from 0.650 V to 0.708 V [49]. In the counter electrode, fabrication of three-dimensional nanostructure is ongoing. The increased surface area of counter electrode not only offers more locations for I_3^- reduction, but also shortens the redox couple diffusion length. Fisher's group prepared a vertically aligned carbon nanotube counter electron for their DSSC device. An increase of short-circuit current was achieved compared to the conventional Pt counter electrode [50]. Since redox couple reduction at counter electrode is not the rate-determining step in the operation of DSSC, improvements of the working electrode nanotructures, dyes and the redox mediators are still the main research focus.

Another way for increasing the efficiency is via new dye synthesis, with higher photon absorption coefficients and a wider spectral response to red spectrum. These types of dyes are also named as panchromatic sensitizers. Gratzel predicted that a broader photon harvesting close to 920 nm would produce a larger short circuit current, from the present value of 20.5 to 28 mA / cm^2, leading to a higher efficiency of 15 % [51]. Recently an efficiency of 12% has been achieved by Diau's Group [10]. Semiconductor quantum dot sensitizers belong to the panchromatic dyes. They all belong to II-VI and III-V groups. Their band gaps are tunable, resulting from the changeable size in nano scale (quantum size effect). PbS for example, can be adjusted to match a gap value of 1.35 eV, a broader response to the red spectrum.

2.3 Previous Work to Increase the Stability

Since the dye-sensitized solar cells (DSSCs) with liquid electrolyte lack long term stability, attempts have been made to replace the electrolyte by other materials, such as nonvolatile gel-like polymer electrolyte or solid hole-transporting materials, the latter present a higher hole conductivity.

Generally, the gel-like polymer electrolyte is a system which is made of a polymer network inflated with liquid electrolytes [11]. Gel-like polymer electrolyte containing DSSC is also named as quasi-solid-state DSSC. It shows better durability than liquid electrolyte, and keeps the high ionic conductivity. Wang *et al*. fabricated a DSSC with polymer gel electrolyte having an efficiency of ~6 % in 2003. The device passed the stability examination under extreme conditions, *e.g.*, light soaking at 60 ^{o}C for 1000 hours and thermal stress at 80 ^{o}C for 1000 hours [52].

In order to completely avoid the leakage problem of the liquid electrolyte, the solid-state hole conductor has been introduced into DSSC system in the late 1990s. This type of DSSC was also named as solid-state dye-sensitized solar cells. In solid-state DSSCs, the solid hole conductors reduce oxidized dye molecules by hole hopping or hole diffusion, which is different from the DSSC with liquid electrolyte [9].

There are two types of hole conductors, organic and inorganic. Organic hole conductors have two categories, small molecule based and polymer based [9]. Small molecule based hole conductors are easier to penetrate into the nano-sized pores and form a good connection with TiO_2. In 1998, Gratzel's group utilized amorphous organic hole conductor 2,2',7,7'- tetrakis (N,N-di-p-methoxyphenyl- amine) 9,9'-spirobifluorene (MeOTAD) in solid-state DSSC.

Though high photon-to-electron conversion efficiencies were observed, the overall power conversion efficiency was 0.74 %, due to the imcomplete pore filling [8]. Now the efficiency has been improved to around 5 % [53], due to the optimization of the nanostructure. The polymer based hole conductors, *e.g.*, dibromo-3, 4-ethylenedioxythiophene (DBEDOT) [54] and polyanilines [55] have the advantages such as low cost, simple fabrication of various nanostructures [54]. However, the poor pore filling issue remains a challenge for DSSCs, due to the large size of the polymerized molecules [54]. Besides, they are unstable when exposed to air or high temperature [25].

Inorganic hole conductors, *e.g.* CuI and CuSCN also show a comparable efficiency of 4.7 % [56] and 2 % [57], respectively, to the organic hole conductors. But the central copper ion is easily oxidized in the ambient environment, which reduces the device performance gradually. To fabricate efficient solid state DSSCs comparable to those embracing liquid electrolyte, the quasi-solid or solid hole conductors should not only form a good interconnection with the porous working electrode, but also be stable in the air. Several solid hole conductors are thus under investigation in solid-state DSSCs.

To summarize, Table 1 shows the advantages and disadvantages of the hole conductors commonly used in solid state DSSCs, to replace the liquid electrolyte.

Table 1: A comparison of three types of hole conductors used in solid state DSSCs.

Types of Hole Conductors	Advantages	Disadvantages
Inorganic Hole Conductors: CuI, CuSCN, *etc.*	High hole mobility: ~ 40 $\mathrm{cm}^2/\mathrm{V}\cdot s$ [58]	Instability; Degradation due to oxygen [59]
Polymer based Hole Conductors: Polyanilines, DBEDOT, Polypyrrole, Poly(3-hexylthiophene), *etc.*	Low cost; Easy fabrication [55] [54]	Thermal expansion and relaxation, easy decomposition; Bad connection between polymer and TiO_2. [25] [54]; Low hole mobility [60]: $\sim 3\times10^{-4}\ \mathrm{cm}^2/\mathrm{V}\cdot\mathrm{s}$ to $1\times10^{-3}\ \mathrm{cm}^2/\mathrm{V}\cdot\mathrm{s}$
Small molecule based Hole Conductors: MeOTAD, *etc.*	Stable; Low cost. [53]	Low hole mobility: $\sim 1\times10^{-4}\ \mathrm{cm}^2/\mathrm{V}\cdot s$ [9]

Obviously, small molecules are the most promising among the three types. Therefore, another small molecule, copper phthalocyanine (CuPc), which has higher hole mobility ($2\sim3\times10^{-4}\ \mathrm{cm}^2/\mathrm{V}\cdot\mathrm{s}$), is chosen to replace the liquid electrolyte in our study.

Chapter 3 Experimental

In order to analyze the properties of the dye-sensitized solar cell (DSSC) and to improve its efficiency as well as durability, it is crucial to first construct a working device. During the master study, the author of this thesis has spent most of time developing device fabrication procedures following the literature. The flow chart of the fabrication process has been developed and presented in Figure 12. In the following sections, the DSSC fabrication processes will be described and explained according to the flow chart, which include three main steps, working electrode fabrication, counter electrode fabrication, and the assembly of the two electrodes together with liquid electrolyte.

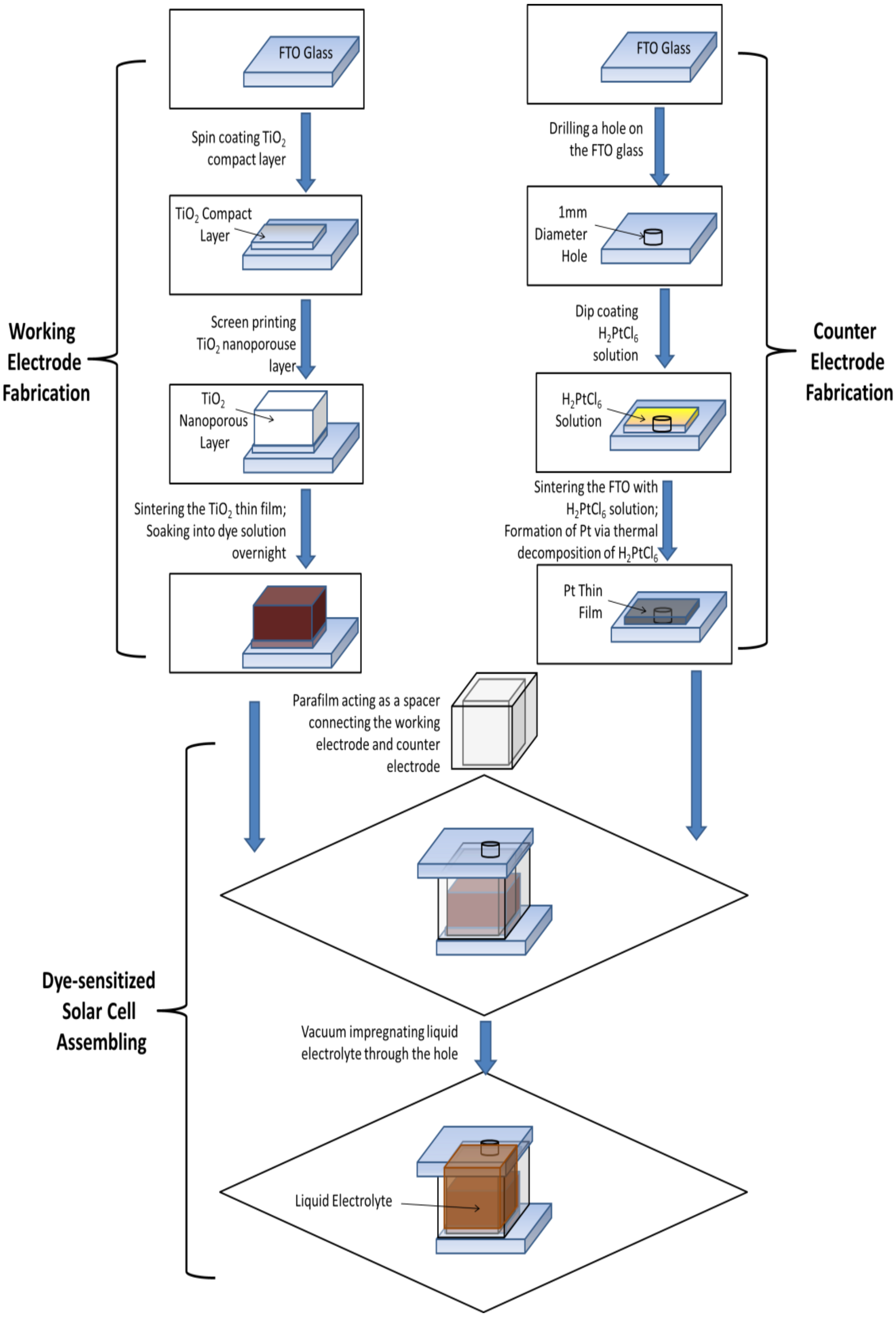

Figure 12: Flow chart of the fabrication of dye-sensitized solar cell.

3.1 Dye-sensitized Solar Cell Construction with Liquid Electrolyte

In general, the procedure of manufacturing a dye-sensitized solar cell (DSSC) including the fabrication of TiO_2 nanoporous working electrode, dye (N719) soaking, preparation of platinum counter electrode, liquid electrolyte (I^-/I_3^-) injection and the final assembly. The preparation of nanoporous TiO_2 working electrode is via sintering the screen printed TiO_2 paste, involving TiO_2 nanoparticles (diameter ~21 nm), acetylacetone as the surfactant and terpineol as the organic binding.

3.1.1 Working Electrode Preparation

Working electrode consists of two layers of titanium dioxide: compact layer (to prevent short-circuit condition) and nanoporous layer (to increase surface area), and the latter serves as a key component in dye-sensitized solar cell.

The fluorine doped tin oxide (FTO, SnO_2: F, 14 Ω/square, Luminescence Technology Corp.) is chosen to be the transparent conductive substrate, because of its stability under high temperature during sintering. Before TiO_2 deposition, a cleaning procedure of FTO is necessary, to reduce interface resistance due to surface dust and to reduce surface tension. The cleaning procedure is listed as follows:

a. Put FTO glasses in ultrasonic detergent solution (Hallmanex II, powerful alkaline concentrate for cleaning cuvettes and optical parts, purchased from Hellma GmbH & Co. KG) (Volume ratio: detergent *versus* deionized water = 1:50) for 30 minutes, to remove the dirt particles on the FTO surface, as well as to decrease the surface tension.

b. Rinse FTO with deionized (DI) water and perform ultrasonic treatment in DI water for 15 minutes. Repeat the step b twice.

c. Rinse with acetone and perform ultrasonic treatment in acetone for 15 minutes.

d. Rinse with isopropyl alcohol and perform ultrasonic treatment in IPA for 15 minutes.

e. Use compressed air to quickly dry the surface of the glasses and put them in the oven at 85 ^{o}C.

f. Treat in UV ozone, in order to eliminate the residual organic layer on the surface of glass.

After the cleaning procedure, FTO glass is ready for TiO_2 compact layer deposition. The compact layer was prepared by spin coating the suspension of titanium dioxide with a diameter less than 25 nm (Titanium (IV) oxide, anatase, nanopowder, <25 nm particle size, $\geq$99.7% trace metal basis, Sigma Aldrich) in anhydrous ethanol 40 s at around 2000 rpm. To form the suspension, add 5 mL anhydrous ethanol into 0.5 g titanium dioxide (diameter<25 nm). Use a spin bar to stir the suspension fiercely for 5 hours. Before spin coating, stir the solution for 1 hour.

After the deposition of the compact layer, nanoporous layer was prepared by screen printing of the TiO_2 paste, according to the reference [32]. The steps are shown below.

a. Add 0.25 g P25 TiO_2 (Titanium (IV) oxide, 70 % anatase, nanopowder, ~21 nm particle size, $\geq$99.5 % trace metals basis, Sigma Aldrich) into a mortar.

b. Drop 0.4 mL acetylacetone (Reagent Plus ≥99 %, Sigma Aldrich) into mortar and grind the power for 5 minutes. Acetylacetone can help to prevent the aggregation of TiO_2 nanoparticles.

c. Drop 0.4 mL DI water into mortar and grind for 5 minutes. Repeat the step twice. Water can also improve the dispersion of TiO_2 nanoparticles.

d. Drop 0.4 mL anhydrous ethanol into mortar and grind fiercely. Repeat the step fifteen times.

e. Drop 0.1 mL anhydrous ethanol into mortar and grind fiercely. Repeat five times.

f. Add 0.83 g *α*-terpineol (96% solution, purchased from Alfa Aesar) into the mixture. Having a high boiling point (above 200 ^{o}C) at normal pressure, terpineol plays an important role in keeping nanoporous structure during the beginning of sintering.

g. Add 1.25 g ethyl-cellulose ethanol solution (0.125 g ethyl-cellulose in 1.125 g anhydrous ethanol). Perform ultrasonic treatment to the mixture for 6 minutes with a break every 2 seconds. As a kind of organic binder, ethyl-cellulose is used to avoid the formation of cracks.

h. Mill the suspension with a hair dryer blowing aside, in order to evaporate ethanol and water faster. The remaining paste should only involve TiO_2, ethyl-cellulose and terpineol. The concentration of TiO_2 in the mixture is essential to the control of thin film thickness during screen printing.

i. Screen-print the TiO_2 paste, on top of the compact layer. The square of the working electrode is 1 cm×1 cm, depending on the aperture of the screen printer. Figure 13 shows a schematic illustration of screen printing. Spread a small amount of TiO_2 paste at the edge of the aperture first. When the squeegee is moved forward, the paste will be spread across the aperture and TiO_2 thin film will be printed on the substrate. The area of TiO_2 thin film is 1 cm×1 cm.

j. Put the double-layer TiO_2 thin film in fume hood for 6 minutes, to increase the surface regularity.

k. Dry on the hot plate at 125^{o}C for about 5 minutes, slowly eliminating the residual water and ethanol.

l. Gradually increase the temperature from 125 ^{o}C to 450 ^{o}C (30 ^{o}C/min). Sinter the TiO_2 thin film at 450 ^{o}C for 15 minutes, and 500 ^{o}C for 15 minutes. The thickness of the thin film can be measured by depth profile instrument in the clean room, at McMaster University.

m. Gradually cool down in the air to 80 ^{o}C, and soak it in N719 dye solution (0.3 M N719 in anhydrous acetyl-acetone) overnight, in order to let the dye be fully adsorbed on the TiO_2 nanoporous structure.

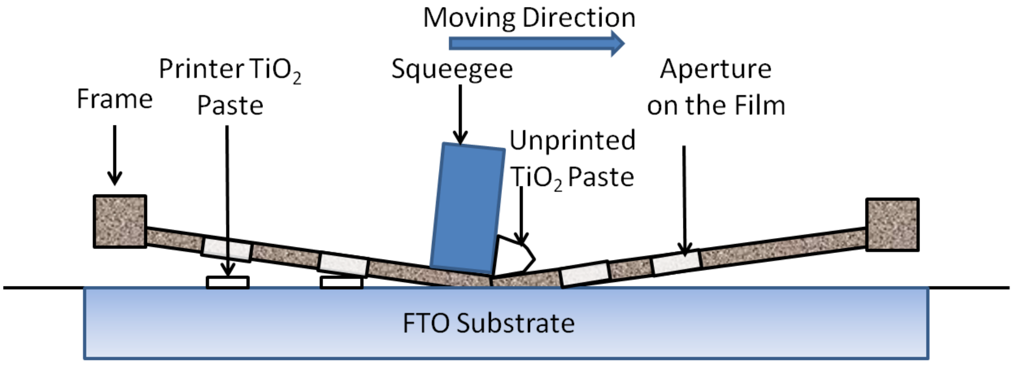

Figure 13: Schematic illustration of screen printing. By moving the squeegee from left to right, the TiO_2 paste will be printed in sequence.

3.1.2 Counter Electrode Preparation

Counter electrode can be prepared in parallel to the working electrode deposition. It involves hole drilling and platinum (Pt) deposition. The procedure is detailed as follows.

a. Drill a hole with 1 mm diameter on FTO glass, by a driller with diamond birr. Liquid electrolyte is injected through this hole in to the DSSC.

b. Clean the FTO glass following the steps stated previously.

c. Remove the surface organic layer by UV ozone treatment for 18 minutes.

d. Place the FTO glass on the hot plate.

e. Drop one dip of the mixture of chloroplatinic acid solution (H_2PtCl_6, 8wt.% in H_2O, Sigma Aldrich) and anhydrous ethanol solution (volume ratio: H_2PtCl_6 : anhydrous ethanol = 1:20, or 2 mg Pt in 1 mL ethanol) on top of the FTO glass, with a gently increasing temperature of the hot plate till 400^oC and keeping for 15 minutes. During sintering, the color of H_2PtCl_6 changes from light yellow to gray. Platinum is deposited on FTO via thermal decomposition of H_2PtCl_6 above 400^oC.

3.1.3 Electrolyte Preparation

Before dye-sensitized solar cell assembling, liquid electrolyte with I^-/I_3^- redox couple was prepared.

a.Dissolve 0.5 M potassium iodide (KI) and 0.05 M iodide (I_2) into acetonitrile and anhydrous ethanol (volume ratio: 85:15).

b. Treat in ultrasonic water bath for 5 min, with an aluminum foil covering the outside of the bottle, in order to prevent UV degradation on electrolyte.

3.1.4 DSSC Assembly

After the preparation of working electrode, counter electrode and electrolyte, they are ready to be assembled into a sandwich structure and a functional DSSC. The procedure of device assembly is described as follows (see Figure 12).

a. Rinse the dye coated working electrode by anhydrous ethanol, in order to remove the over aggregated dye molecules and leave monolayer on top of nanoporous TiO_2.

b. Dry the working electrode.

c. Place a Para-film spacer with an aperture 1 cm×1 cm to connect the working electrode and the counter electrode together, under the pressure from two clips at 80 ^{o}C for 1 minute in an oven. The thickness of the Para-film is around 127 μm. After heated under a pressure, its thickness will be decreased less than 60 μm.

d. Put the device into the vacuum impregnation system (see Figure 14). Drop few droplets of the electrolyte at the back surface of the counter electrode, covering the hole. Vacuum the chamber by mechanical pump. The trapped air in the nanoporous working electrode and in the space between the working electrode and counter electrode will be evacuated under negative pressure. Till no more bubbles come out, turn off the pump and gradually increase the air pressure by the valve. Once coming back to the ambient pressure (760 mm Hg), the electrolyte will be pushed into the space and pores by the pressure difference. (Pay attention to the backflow of the mechanical pump oil. Keep the tube upwards when increasing the pressure of the chamber to the normal level). Vacuum impregnation improves the interpenetration between liquid electrolyte and the nanoporous working electrode.

e. The hole is sealed using crazy glue and a cover glass (0.1 mm thickness), to lower the evaporation rate of the volatile electrolyte.

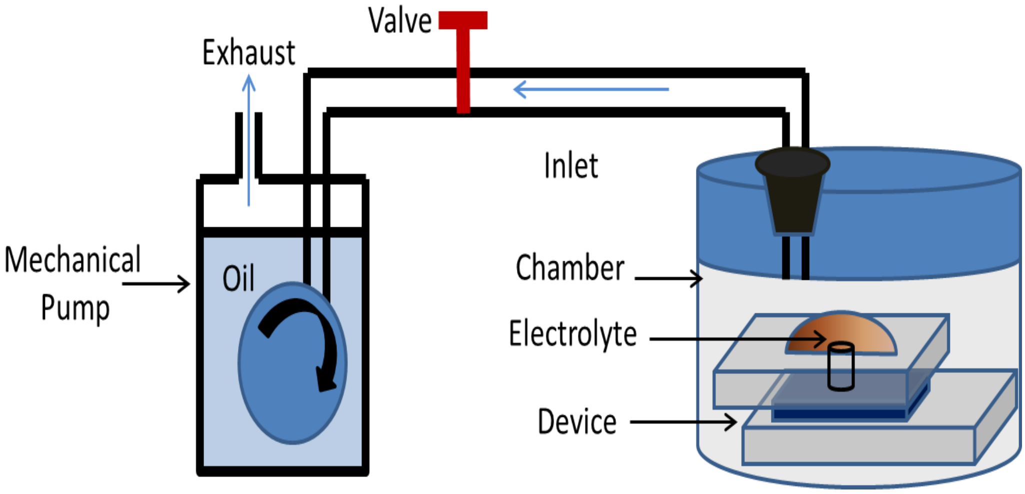

Figure 14: Schematic illustration of vacuum impregnation. When the air is evacuated from the chamber, bubbles can be seen in electrolyte. Once evacuation stops, and the pressure gradually returns to the ambient, electrolyte will be pushed into the device, and more importantly into the nanoporous structure by the pressure difference.

3.2 Dye-sensitized Solar Cell Construction with Solid Hole Conductor

3.2.1 Working Electrode Preparation

The procedure of working electrode preparation is the same as the dye-sensitized solar cells (DSSCs) with electrolyte. Here, patterned fluorine tin oxide (FTO) conducting glass is used as substrate [61], which is necessary to prevent short circuit in solid-state electronic devices. The procedure of patterning is listed as follows. .

a. Sprinkle dry zinc metal (diameter: ~1 mm) over the dry FTO glass.

b. Drop dilute hydrochloric acid on the substrate at room temperature (Volume ration: concentrated hydrochloric acid: DI water=1:2). Zinc powder will react with HCl fiercely.

c. After 3 minutes, wash the etched strip with DI water. Now the FTO glass has been patterned (see Figure 15).

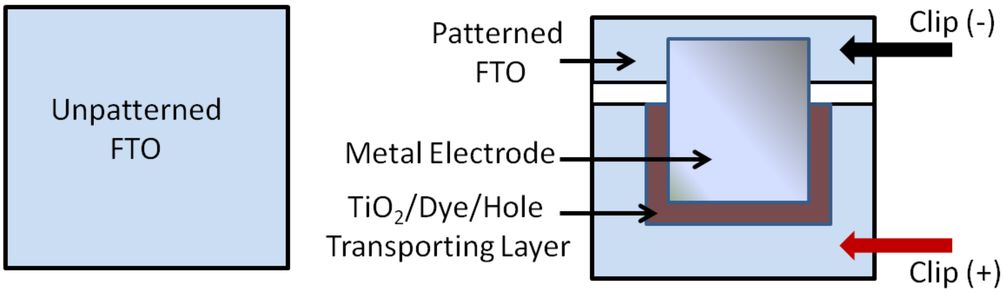

Figure 15: The Pattern of FTO conducting glass and the top view of the solid-state DSSC.

3.2.2 Hole Transporting Layer Preparation

The choice of copper phthalocyanine (CuPc) as hole conductor in the fabrication of solid-state dye-sensitized solar cell (DSSC) will be explained in Section 4.2. CuPc is a widely used p-type small molecule material. The absorption spectra of CuPc are between 600-700 nm (i.e. green and blue lights). Its advantages include high thermal chemical stability, hard to be dissolved in concentrated sulfuric acid (H_2SO_4) [4]. The molecular structure of CuPc is shown in figure 16.

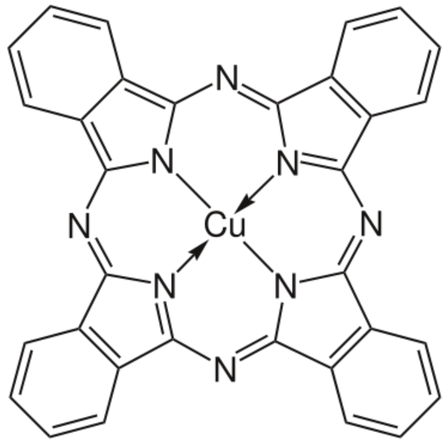

Figure 16: Molecular structure of CuPc [4].

The solution processed CuPc thin film was prepared according to Wang's Ph.D. Thesis [4], as shown in the following procedures.

a. Dissolve 10mg CuPc in 20g concentrated H_2SO_4.

b. After 24 hours, add CuPc - H_2SO_4 mixture drop by drop into 700 ml deionized water with constant magnetic stirring at 3^oC. With the decrease of the concentration of H_2SO_4, CuPc will precipitate. And the low temperature will increase the precipitation rate.

c. Filter the suspension liquid and collect the CuPc nanoparticles by firstly washing with water until pH=5, and with acetone to eliminate the residue water finally.

d. Dry the CuPc nanoparticles with compressed air.

e. Add 1/3 CuPc nanoparticles (~3 mg) into 50 ml toluene, and put it in the ultrasonic water bath for half an hour.

f. Deposit the CuPc nanoparticles on top of the dye coated TiO_2 by spray coating.

3.2.3 Metal Electrode Deposition via Thermal Evaporation

Auminum is deposited on the surface of CuPc via thermal evaporation. Figure 17 illustrates the operating principles. The metal in the boat is heated in high vacuum (~10^{-5} torr) by increasing the applied current. After the metal is melted and evaporated, the atomic beam will hit the substrate and the film grows. The thickness is monitored by a quartz crystal microbalance (QCM). To prevent the metal oxide from deposition at the very beginning, the substrate is shielded by a shutter for a few seconds. When the QCM shows the wanted thickness, block the beam by the shutter again. Vacuum system operational steps are shown in Figure 17.

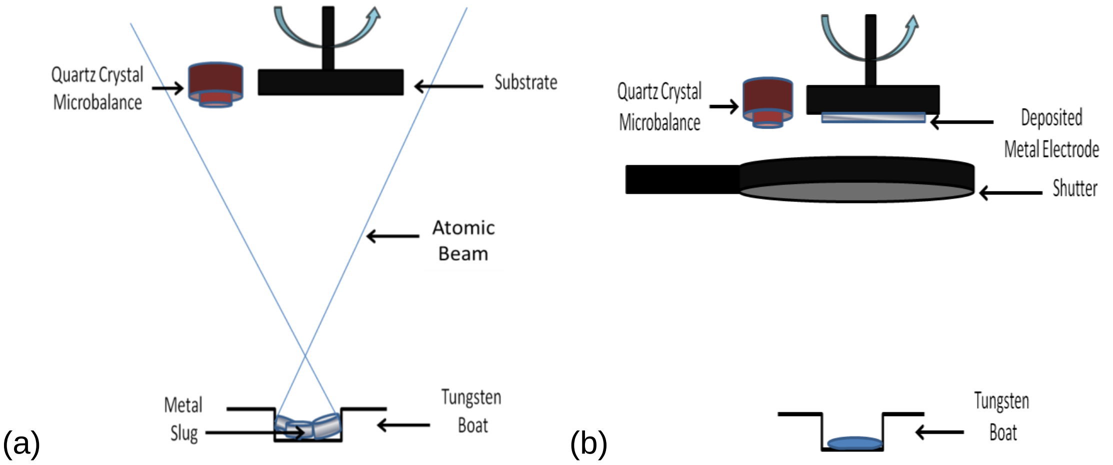

Figure 17: Schematic illustration of thermal evaporation.

(a) During deposition; (b) After deposition.

3.3 I-V Curve Measurement

The performance of the dye-sensitized solar cell was evaluated by the I-V curve measurement under the illumination intensity of 100 mW / cm^2. The applied voltage was controlled by the potentiodynamic 'POTDYN.exp' scrip in the CMS100 system (Corrosion Measurement System, Gamry Instruments, Inc.). The experimental setup is shown in Figure 18.

The CMS100 system has been installed in a personal computer, and has five external cables connected to the measurement system. The five cables are labeled as working, working sense, reference, counter and ground, painted in green, blue, white, red and black, respectively. During the measurement, the black ground cable is usually kept floating.

The sweeping potential ranged from -0.2 V to +0.8 V. In a typical measurement, the reference cable (White) should be connected to the cathode of the solar cell to collect electrons, which is the FTO glass coated with TiO_2 and dye. The counter cable (Red) should be clipped together with the reference cable, according to the equivalent circuit. The other two cables working (Green) and working sense (Blue) were both clamped to the device anode, which was the platinum coated FTO glass or the metal electrode, to transport electrons back to the solar cell.

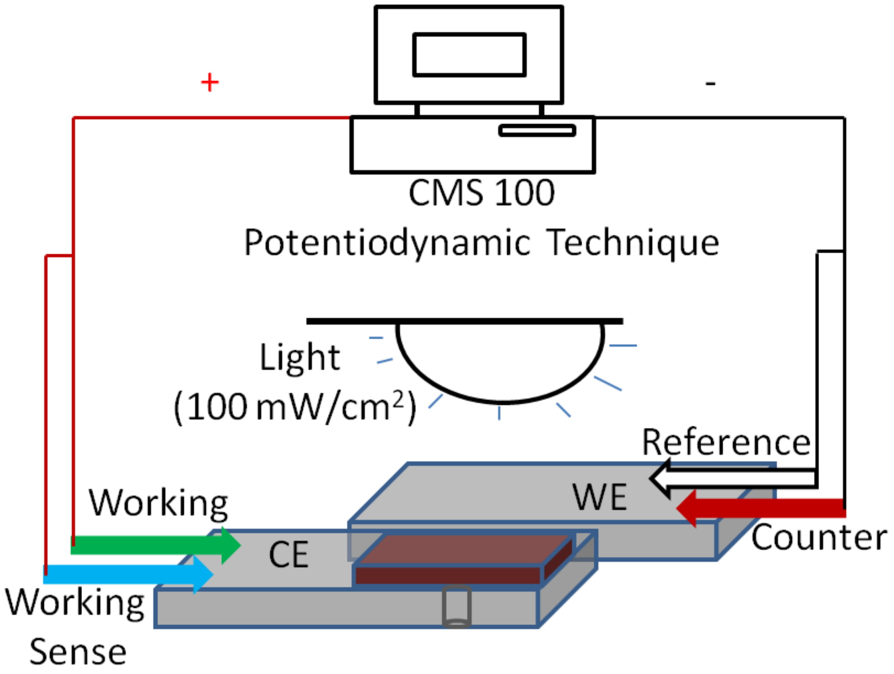

Figure 18: The experimental setup for I-V curve measurement.

3.4 Scanning Electron Microscopy (SEM) Measurement

The surface morphology measurement was performed with a scanning electron microscopy (SEM) (JEOL 7000F, Canadian Centre for Electron Microscopy) to obtain data on nanoparticles agglomeration and pore size. A piece of screen printed TiO_2 thin film (~12 μm) with the FTO conducting glass was mounted to the metal stub by double faced carbon tape. A small amount of silver paste is added between the edge of the FTO conducting glass and the stub for an improved conductivity. In our SEM characterization, platinum coating on TiO_2 nanopowders was not employed, as it blocks important surface information. To avoid charging by the electron beam with high energy, low accelerating voltage (1 kV) of the electron beam and low beam current (2 μA) was chosen during the characterization.

3.5 X-ray Diffraction (XRD) Measurement

Characterization of crystals, *e.g.* phase phase identification, texture analysis, percent crystallinity, particle (grain) size and thin film analysis [62], was performed by X-ray diffraction (XRD) at room temperature on a Bruker Smart 6,000 CCD 3-circle D8 diffractometer with a Cu RA(Rigaku) X-ray source (wavelength=1.5418 Angstrom) (McMaster Analytical X-Ray Diffraction Facility). Cross-coupled parallel focusing mirrors were used to monochromate the X-ray radiation. The data were collected at still mode with 300 s per frame and processed with GADDS (General Area Detector Diffraction System) software.

XRD characterization has built a bridge between the real space and the reciprocal space. In XRD experiment, the wavelength of a typical X-rays is around 1.5 angstrom, which is approximately the magnitude of the spacing of lattice planes in crystals. When an incident beam of monochromatic X-ray hits a sample, whether crystalline or amorphous, scattered X-rays with the same wavelength as the incident X-ray are generated, as they leave the sample. The phenomenon is called as X-ray diffraction. The electron distribution in the sample results in the uneven intensities and spatial distribution of the scattered X-rays. Therefore, once the patterns of the scattered X-rays are detected, the structure of the sample can be determined, through Fourier transformation [63].

In real space, constructive interference takes place if the distance of the adjacent lattice planes (d-spacing) and the incoming wavelength λ satisfies the Bragg Law [62]:

$$\mathrm{n}\lambda = 2\mathrm{d}\sin\theta \tag{3.1}$$

Where θ is the incident and reflection angle, also called the Bragg angle, at which a diffraction peak is shown; n is an integer number, representing the order of reflection. A schematic illustration of Bragg Law is shown in Figure 19.

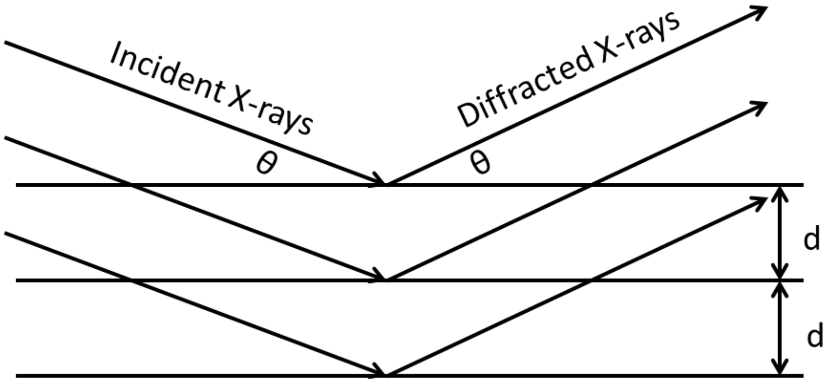

Figure 19: Schematic illustration of Bragg Law.

In our XRD characterization, two-dimensional (2-D) area detector has been utilized in the characterization, to acquire more complete crystal information than the diffraction intensity *versus* 2θ plot [64], where crystallite orientation cannot be obtained as efficiently.

.

Chapter 4 Results and Discussion

4.1 Duplicating DSSC with Liquid Electrolyte

One of the main challenges in the field of DSSC is that the devices with liquid electrolyte lack long term stability because of the volatility of the electrolyte and assembly problems, which decrease the device performance.

To confirm the instability of DSSC with liquid electrolyte, a DSSC was duplicated at McMaster University (*cf*. Section 3.1 for detailed procedures), and followed by I-V characterization. The overall structure of the device is: FTO/ TiO_2 compact layer (~20 nm) / TiO_2 nanoporous layer (~12 μm) / N719 dye (~1 nm) / electrolyte (I^-/I_3^- redox couple) (~50 μm) / Pt counter electrode (~10 nm)/ FTO, as shown in Figure 20.

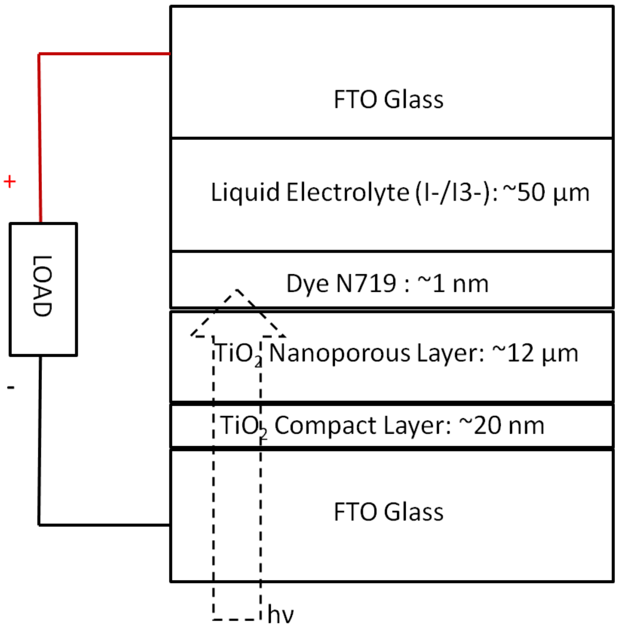

Figure 20: Device structure of the DSSC with liquid electrolyte.

The I-V curves of the DSSC with liquid electrolyte obtained by the

CMS100 system (Section 3.3) under the illumination intensity of 100 mW / cm^2 have been shown below (Figure 21). The solid line was obtained right after the device was fabricated. The dashed I-V curve was measured after two hours. The short-circuit current (J_{sc}) decreased from 4.18 mA / cm^2 to 2.64 mA / cm^2 in two hours. The open-circuit voltage (V_{oc}) also experienced a small reduction from 0.535V to 0.52V. Correspondingly, efficiency of the same device dropped from 0.74% to 0.52%. As a result, the dye-sensitized solar cell (DSSC) with liquid electrolyte was duplicated and the instability of it was verified.

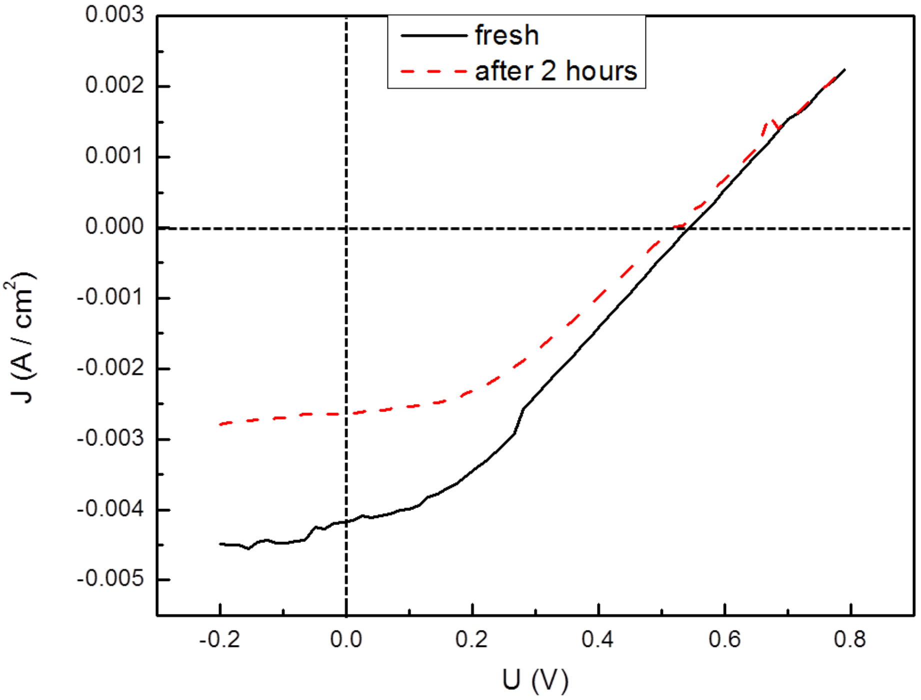

Figure 21: I-V curves of DSSC with liquid electrolyte (illumination intensity: 100 mW / cm^2). The solid curve was measured right after the device was fabricated. The dash curve was measured after two hours.

The photovoltaic parameters of our DSSC with liquid electrolyte were summarized in Table 2. Without sophisticated sealing technique, the photovoltaic parameters decreased within two hours.

Table 2: Photovoltaic parameters of a DSSC with liquid electrolyte, data obtained right after the device was fabricated and after two hours.

Measurement Time	V_{oc} (V)	J_{sc} (mA / cm^2)	Power Conversion Efficiency
Right after fabrication	0.535	4.18	0.74%
After 2 hours	0.520	2.64	0.52%

4.2 Replacing Liquid Electrolyte with Solid Hole Conductor (CuPc)

In Section 4.1, it was verified that a DSSC with liquid electrolyte degrades fast, probably due to the volatile electrolyte and assembly problems. Replacement of the volatile liquid-state electrolyte with solid-state hole conductor becomes necessary. A small molecule based hole conductor, copper phthalocyanine (CuPc, molecular structure shown in Figure 16, Section 3.2.2), is used here to replace the liquid electrolyte.

One reason to choose CuPc as a hole conductor is, because its band gap [4] [25] matches with the band gap of the other components in solid-state DSSC [14]. Figure 22 shows the band diagram of the solid-state DSSC with CuPc. The open-circuit voltage of CuPc solid state DSSC is defined as the difference between the conduction band of TiO_2 (~ -0.5 V *vs*. NHE) and the highest occupied molecular orbital (HOMO) level of CuPc (~ 0.8 V *vs*. NHE). Besides, the HOMO level of CuPc offers a driving force of 0.3 V for the oxidized dye regeneration (D/D^+: ~1.12 V *vs*. NHE). Other advantages of CuPc also include high thermal and chemical stabilities, as well as low cost [4].

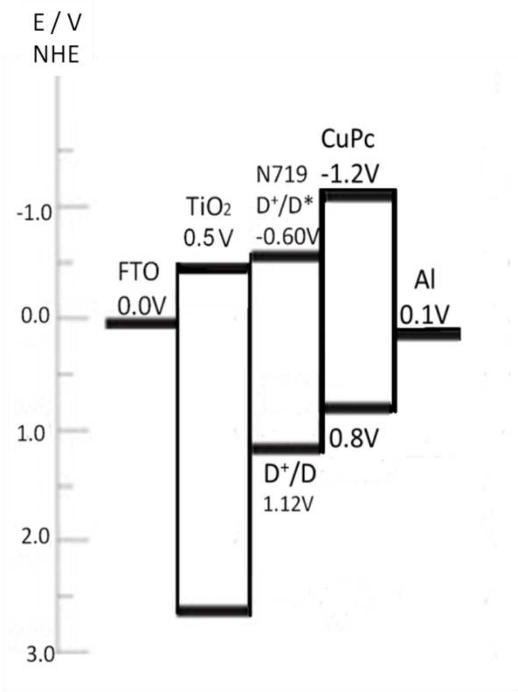

Figure 22: Band diagram of the solid-state DSSC with CuPc as hole conductor. The highest occupied molecular orbital (HOMO) level of CuPc is ~0.8 V (*vs*. NHE), and the lowest unoccupied molecular orbital (LUMO) level is ~ -1.2 V (*vs*. NHE) [14]. CuPc reduces the oxidized dye N719 by transporting holes in its HOMO level from N719 to Al.

The overall device structure is thus as follows: FTO/ TiO_2 compact layer (~20 nm) / TiO_2 nanoporous layer (~12 μm) / Dye N719 (~1 nm) / CuPc hole conductor layer (~2 μm) / Aluminum metal electrode (~100 nm) (see Figure 23). The I-V curve of the new solid-state DSSC was obtained from the CMS100 system under the illumination intensity of 100 mW / cm^2, as shown in Figure 24. The open-circuit voltage of the CuPc solid state DSSC was found to be 0.515 V. However, a low short-circuit current of only 0.008 mA / cm^2 was obtained, far below than that of the DSSC with liquid electrolyte (see Section 4.1).

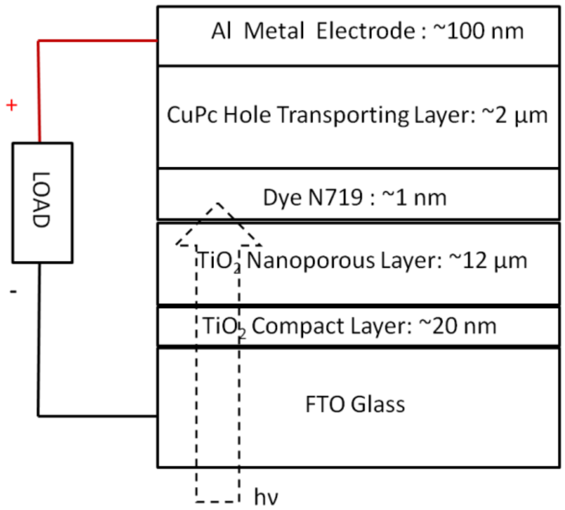

Figure 23: Device structure of the solid-state DSSC of CuPc as hole conductor.

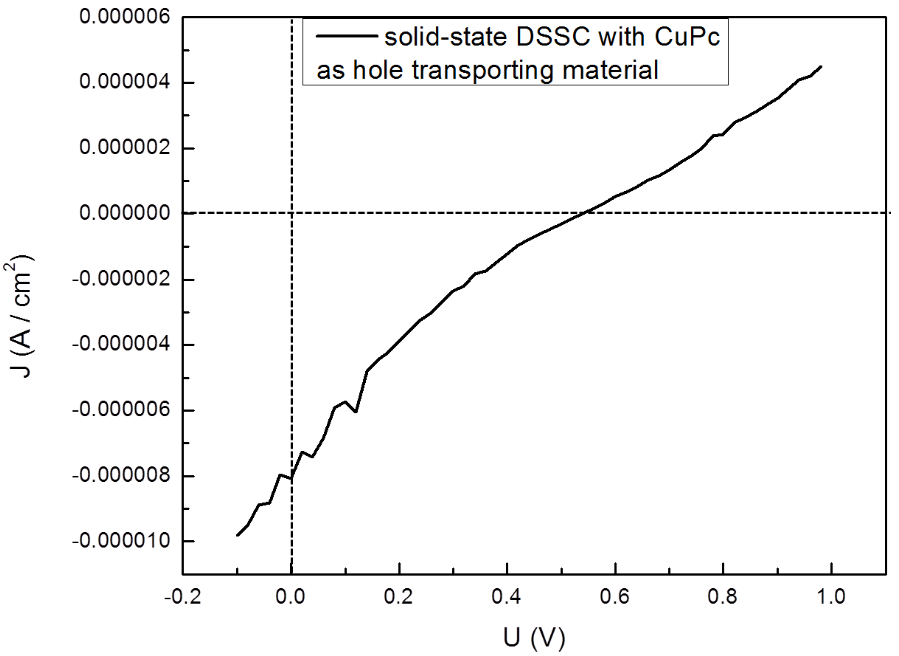

Figure 24: I-V curve of the solid-state DSSC with CuPc as hole conductor (illumination intensity: 100 mW / cm^2).

The unsatisfactory short-circuit current found from the CuPc solid-state DSSC could result from a poor hole transport in the CuPc thin film. It is thus necessary to learn the fundamental carrier transport mechanism in the CuPc thin film.

In brief, there are two mechanisms for hole transport in CuPc thin films, intra molecule transport and inter molecule transport. The former is via *π-π* overlap in a molecule. The latter is through *π-π* stacking at delocalized sites, or through hopping at localized sites [65].

Both the hole transport mechanisms are closely related to the CuPc crystal structure and the molecule arrangements in the thin film. Therefore, it is essential to investigate the crystal structure of the CuPc thin film, in order to find out the cause of the unsatisfactory device performance (Section 4.2). We employed 2D grazing incidence XRD to characterize the crystal structure, phase composition and molecule arrangement of the solution processed CuPc thin films. Such a characterization is described in a published paper in a refereed journal of *Crystals* [66], which comprises the main content of the next section.

4.3 Investigating Phase and Texture of CuPc Thin Films by 2D Grazing Incidence XRD

PAPER: Phase and Texture of Solution-Processed Copper Phthalocyanine Thin Films Investigated by Two-Dimensional Grazing Incidence X-Ray Diffraction, **Crystals** *1*, 112 (2011)

Lulu Deng [1,*], Kewei Wang [1], Cindy X. Zhao [1], Han Yan [1], James F. Britten [2] and Gu Xu [1,*]

[1] Department of Materials Science and Engineering, McMaster University, 1280 Main St. W., Hamilton, Ontario, L8S4L7, Canada; E-Mails: wangk25@mcmaster.ca (K.W.); zhaox8@mcmaster.ca (C.X.Z.); yanh@mcmaster.ca (H.Y.)

[2] Department of Chemistry and Chemical Biology, McMaster University, 1280 Main St. W., Hamilton, Ontario, L8S4M1, Canada; E-Mail: britten@mcmaster.ca

* Authors to whom correspondence should be addressed; E-Mail: dengl2@mcmaster.ca (L.D.); xugu@mcmaster.ca (G.X.); Tel.: +1-905-525-914 ext. 23317 or 27341.

Abstract: The phase and texture of a newly developed solution-processed copper phthalocyanine (CuPc) thin film have been investigated by two-dimensional grazing incidence X-ray diffraction. The results show that it has β phase crystalline structure, with crystallinity greater than 80 %. The average size of the crystallites is found to be about 24 nm. There are two different arrangements of crystallites, with one dominating the diffraction pattern. Both of them have preferred orientation along the thin film normal. Based on the similarities to the vacuum deposited CuPc thin films, the new solution processing method is verified to offer a good alternative to vacuum process, for the fabrication of low cost small molecule based organic photovoltaics.

Keywords: solution processing; copper phthalocyanine; grazing incidence X-ray diffraction

(Part of the long introduction is not duplicated.)

4.3.1 Introduction

Dye sensitized solar cells (DSSCs) with liquid electrolyte lack long term stability because of the volatility of the electrolyte and assembly problems, thus, a small molecule based hole conductor, copper phthalocyanine (CuPc) is chosen to replace the liquid electrolyte, for its intrinsic thermal and chemical stabilities. However, the solid-state DSSC with CuPc shows a low short-circuit current, which is closely related to the inefficient hole transport in the CuPc thin film. The application of X-ray diffraction (XRD) analysis is necessary to fully characterize the crystallite phase and orientation information, which is crucial in hole transportation [67]. To accomplish this goal, grazing incidence X-ray diffraction (GIXRD) has been used, since it offers more direct information than, *e.g.*, selected area electron diffraction performed by transmission electron microscopy [68] , where the crystal structure and orientation cannot be obtained without the substrate removal. In addition, a two-dimensional (2-D) area detector has been employed here, to obtain more complete crystal information than the diffraction intensity *versus* 2θ plot [64], where crystallite orientation cannot be obtained as efficiently.

It is therefore the purpose of this report to present crystal phase and orientation studies of our newly developed solution processed CuPc thin film. Various phases can be obtained depending on different processing parameters [69]. In our solution processed β-phase CuPc thin film, two different crystallite fiber orientations ($[20\bar{1}]$ and [001] normal to surface) were found to co-exist, with $(20\bar{1})$ orientation dominating the diffraction pattern. Compared to the vacuum deposited α-phase CuPc thin films with (100) and (110) fiber orientations [70], our new crystalline thin films have similar crystallite sizes [71] [72]. The similarities clearly show that the new solution processing method offers an excellent alternative to vacuum process, for the fabrication of low cost small molecule based solar cells.

4.3.2 Crystal Structure of Solution-processed CuPc Thin Film

Figure 25a shows the two-dimensional (2-D) diffraction pattern of the thin film obtained by grazing incident X-ray (incident X-ray angle at 2°), performed on the newly developed solution-processed CuPc thin film (thickness: ~100 nm) on top of an indium tin oxide (ITO) conducting glass substrate (ITO thickness: ~50 nm; glass thickness: ~1 mm). The diagonal from the top left to the bottom right shows the side view of sample holder (Figure 25a). The frame shows strong diffraction spots from four sets of lattice planes, with 2θ peak width varying between 0.4° and 1.1°. The chi spread of (001) is 18.7°, and 28.8° for ($20\bar{1}$), obtained by GADDS software [63]. Very weak ($00\bar{1}$) signals can be observed in Figure 25a near the plane of the thin film. The crystallinity of the thin film is found to be greater than 80 %, calculated again by GADDS software [63] .

While these diffraction features are produced by the reciprocal lattice points intercepting the Ewald sphere, they do not necessarily represent a single crystal, due to the arbitrary choice of φ angle. Because the typical diffraction pattern does not vary with φ (Figure 25b), the spots in Figure 25a actually represent polycrystalline fiber-type arrangements, with a preferred orientation along the thin film normal (from the center to the upper–right), and random crystallite orientation in the plane of the film.

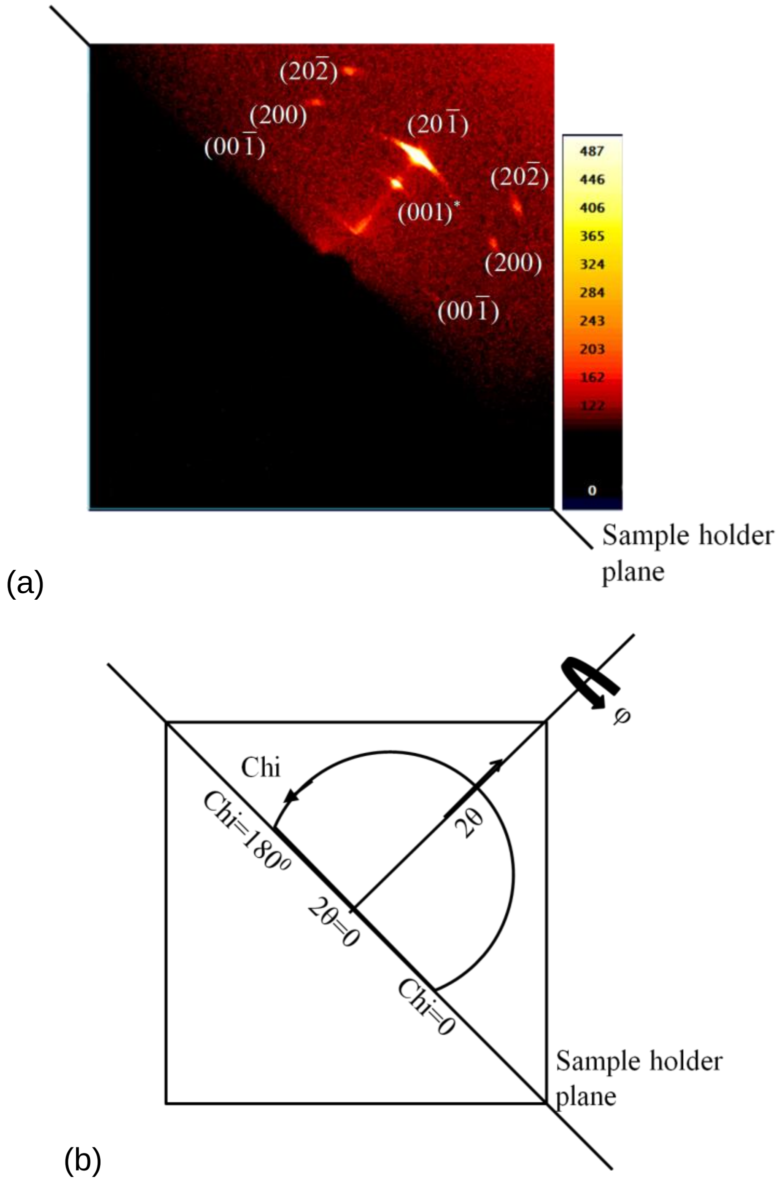

Figure 25: (a) Two-dimensional grazing incidence X-ray diffraction image obtained with the incident X-ray almost parallel to the surface of the solution-processed copper phthalocyanine (CuPc) thin film (incident X-ray angle at 2°). The dark shadow results from using a fixed goniometer (χ_g = 54.7°). (b) The geometry definition of the angles related to the location of the diffraction patterns.

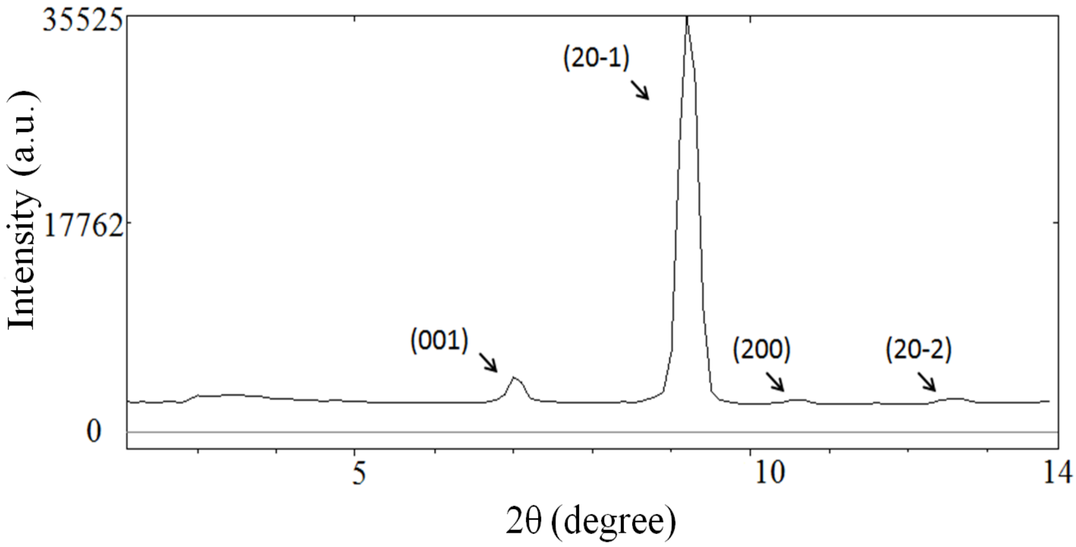

Figure 26: Diffraction intensity *versus* 2*θ* plot (obtained by the integration of Chi (0–180°) with GADDS software [63] and PowderCell software [73]

To analyze the phase composition, do the integration of chi from 0 to 180^{o} and achieve the diffraction intensity *versus* 2*θ* plot (Figure 26) by using GADDS software [63] and PowderCell software [73]. The solution-processed CuPc has been determined to be the *β* phase. The lattice parameters are as follows: a = 19.407 *Å*, b = 4.7900 *Å*, c= 14.628 *Å*; *β* = 120.560° ± 0.003°, *α* = *γ* = 90°; non-standard space group: $P2_1/a$, Z=2 [69] [74]. The four peaks (Figure 25) represent the (001), (20$\bar{1}$), (200) and (20$\bar{2}$) lattice planes, located at 2*θ* of 7.03°, 9.21°, 10.59° and 12.54°, respectively. [69]. The average crystallite size is found to be about 24 nm, calculated from the full width at half-maximum (FWHM = 0.35°) of the peak at 2*θ* of 9.21°, using the Debye-Scherrer formula [75]. This is correlated to Wang's results obtained from scanning electron microscopy (SEM) [4]. Compared to the *α*-CuPc thin film usually obtained by vacuum deposition, the *β*-CuPc phase obtained by the solution process is a more thermodynamically stable structure, which is usually formed above

210 °C or under the influence of organic solvents [69]. However, the hole conductivity of *β*-phase CuPc is 2×10^{-6} S/m, which is two orders of magnitude lower than that of the *α*-CuPc [76].

4.3.3 Preferred Orientation of the CuPc Crystallites

As described above, the thin film had strong textures (highly preferred orientations of crystallites), as shown by the limited Chi intensity distribution.

To analyze the preferred orientation, the intensity distribution of each lattice plane with respect to the sample coordinates in stereographic projection was plotted (using GADDS software [63], assuming fiber geometry), as a pole figure. As shown by the three-dimensional (3-D) surface plot of the $(20\bar{1})$ pole figure (Figure 27a), enhanced pole intensity (marked with brighter color) is located exactly in the center of the figure. It reveals that the *β*-CuPc crystallites were oriented with the $(20\bar{1})$ planes parallel to the substrate. In addition, the 3-D surface plot of (001) pole figure (Figure 27b) demonstrates that the (001) planes were parallel to the substrate.

However, within a single crystallite, (001) planes cannot be parallel to $(20\bar{1})$ planes, as they form an angle of 99.656°. Therefore, there must be two different fiber textures coexisting in our thin film. A possible reason for the two types of fiber textures observed is that the arrangement of CuPc crystallites is more stable along (001) and $(20\bar{1})$ directions. The indium tin oxide (ITO) substrate does not affect the fiber textures, since the ITO glass did not receive any further pretreatment except for cleaning, and the ITO glass itself is polycrystalline with no preferred orientation.

Moreover, the four diffraction features in Figure 1a, resulting from (200) and ($20\bar{2}$) planes, correlate with the ($20\bar{1}$) fiber orientation (Figure 27c and d), and represent the intersection of rings of diffraction with the 2-D detector [62]. The weak ($00\bar{1}$) signal near the plane of the thin film in Figure 25a comes from ($20\bar{1}$) fiber orientation as well. As a result, ($20\bar{1}$)-normal orientation dominates the diffraction pattern in Figure 25a. Only a small fraction of crystallites were found to be in the (001)-normal orientation, thus the (200) and ($20\bar{2}$) diffraction intensities were too low to be observed from the crystallites in (001) orientation.

Therefore, it is found that β-CuPc crystallites, in the newly developed thin film, have two preferred orientations with one dominating. A similar situation exists in the vacuum deposited thin film, where the (100) and (110) orientations of the α-phase are the commonly preferred axial orientations [69].

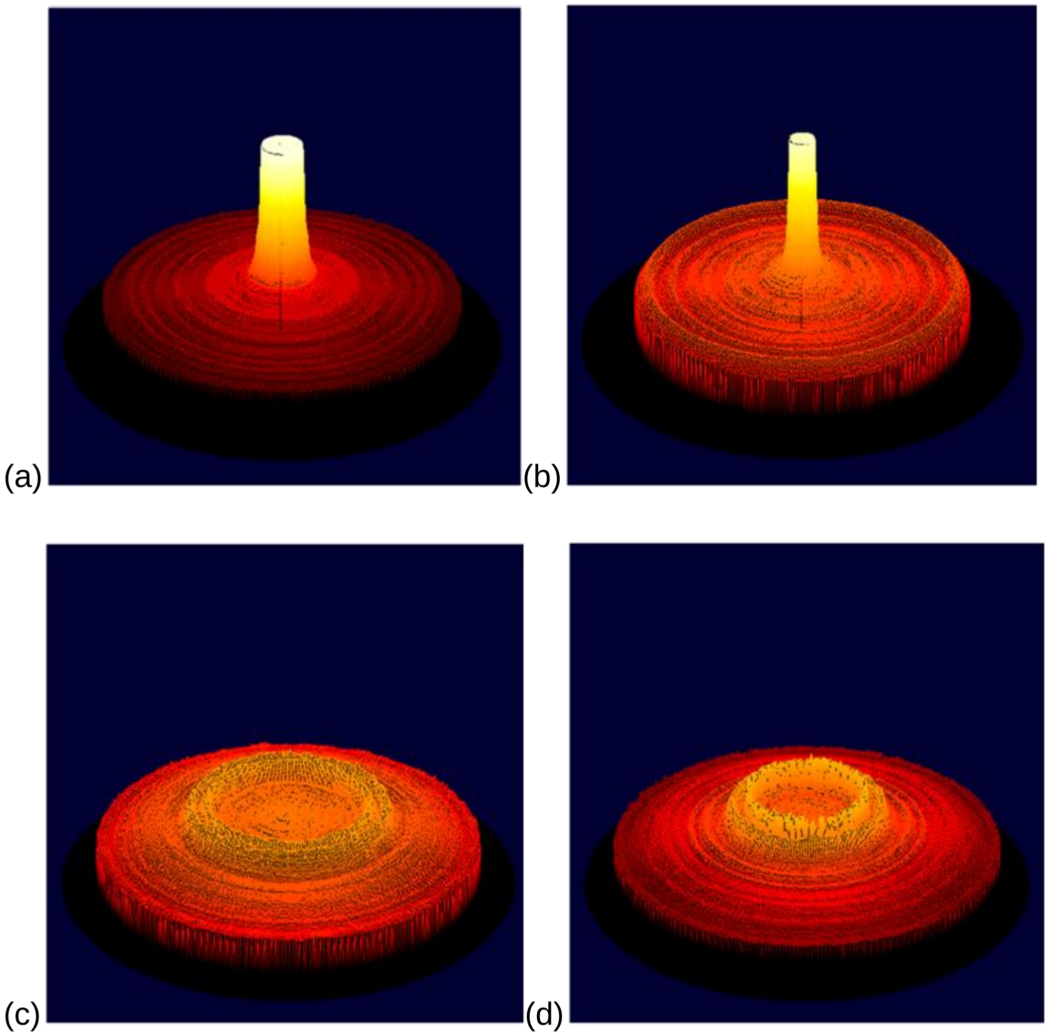

Figure 27: Three-dimensional surface plots of the pole figures (constructed by GADDS software [63]) for the planes (a) $(20\bar{1})$; (b) (001); (c) (200); (d) $(20\bar{2})$.

4.3.4 The Arrangement of CuPc Crystallites in the Thin Film

From the discussion above, it becomes evident that two different types of preferred orientations can be found in the newly developed solution-processed CuPc thin film.The $(20\bar{1})$ and (001) orientations of the crystallites are characterized by the ($20\bar{1}$) and (001) lattice planes parallel to the substrate. Therefore, the molecular arrangements of β-CuPc can be depicted, as shown by Figure 28. The CuPc molecules are square, but when they stack along b axis the cross-section of the 1D chain is not square because of the slant of the molecules. CuPc molecules aggregate as tilted stacks (along [010]), with an almost rectangular cross-section. The wider side of the stacks forms the ($20\bar{1}$) plane, while the narrow side of the stacks defines the [001] direction. A majority of crystallites are arranged in the ($20\bar{1}$) orientation as described by Figure 28a. A minority of crystallites are arranged in the (001) orientation, as illustrated by Figure 28b. The packing of the molecular stacks on their ($20\bar{1}$) surface allows the molecules to lie at a shallower angle to the surface. The only other packing option is for the stacks to rotate approximately 90 degrees on axis and lie on the (001) surface. In this less populated orientation the molecules are at a much higher inclination to the surface.

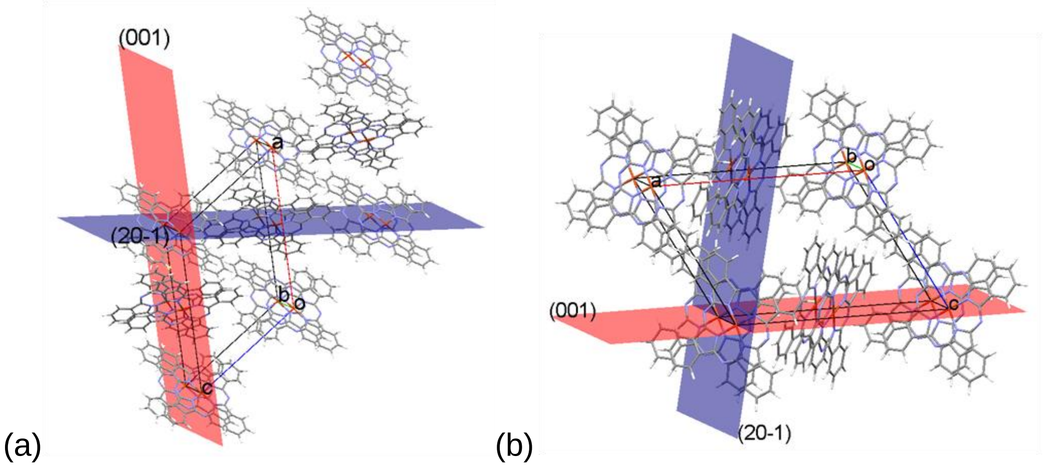

Figure 28: (a) The primary arrangement of CuPc crystallite in the ($20\bar{1}$) orientation; (b) The secondary arrangement of CuPc crystallite in the (001) orientation (CuPc single crystal diffraction information was found in database, and then was input into Mercury 2 [77] to display).

4.3.5 Experimental Section

As for the strategy we used to prepare CuPc thin films, we firstly precipitated CuPc-H_2SO_4 mixture into water to obtain the surfactant-free CuPc nanoparticles. Then, the CuPc nanoparticles were washed by water, dried in a vacuum oven at 70 °C, and were deposited on the substrate by spray coating [78]. Two-dimensional grazing-incidence X-ray diffraction was employed to measure the thin film texture [62]. The orientation distribution of several crystallographic planes over a range of angles was measured simultaneously; in addition the textures were observed directly from the 2-D diffraction frame. Figure 29 shows a schematic illustration of the two-dimensional grazing-incidence X-ray diffraction measurement employed in our experiment.

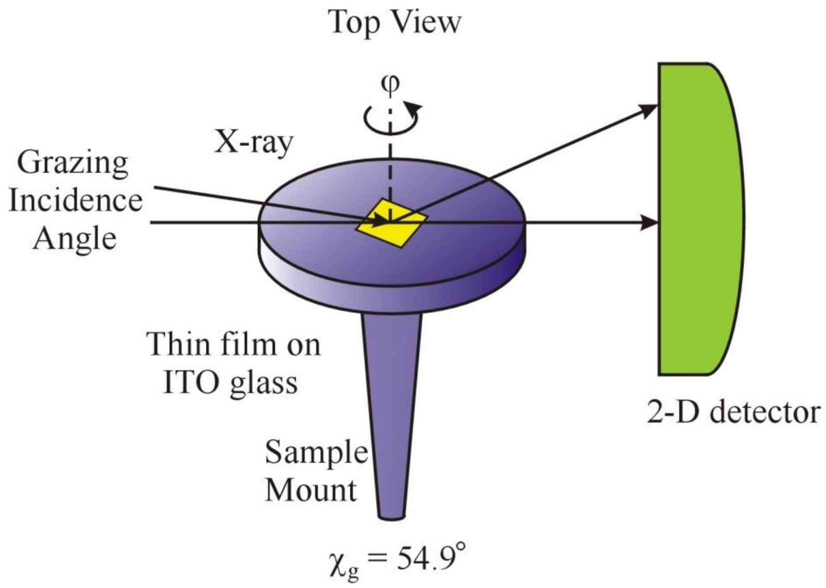

Figure 29: Schematic illustration of two-dimensional grazing-incidence X-ray diffraction (2-D GIXRD) measurement (incident X-ray angle at 2°, a fixed goniometer at $\chi_g = 54.9°$).

The distance between the 2-D detector and the sample mount was 16.715 cm (Figure 29). The experiment was performed at room temperature on a Bruker Smart 6000 CCD 3-circle D8 diffractometer with a Cu RA (Rigaku Ru200) parallel focused X-ray source ($\lambda = 1.5418$ Å). The data were collected at still mode with 300 seconds per frame and processed with GADDS software [63].

Since the 2D diffraction image of our CuPc thin film shows a distribution of orientation, in GADDS software, “External Method” is used for a relative measurement of crystallinity. By determining the boundaries of the amorphous region and crystalline region, with the same 2θ limits and different chi range, the GADDS software can calculate the crystallinity by employing specified areas of frame data [63]. The calculating result shows that the crystallinity of our CuPc thin film is greater than 80%.

4.3.6 Summary

To summarize, the crystalline phase and orientation information has been analyzed for our newly developed solution-processed CuPc thin films by 2-D grazing incidence X-ray diffraction. The results show that the film has a crystallinity greater than 80%, and an average crystallite size about 24 nm, similar to that of the vacuum deposited thin films. In addition, crystallites in the thin film had two preferred orientations $(20\bar{1})$ and (001), with $(20\bar{1})$ dominating. The crystallites in both orientations have a preferential ordering along the substrate normal, and are randomly oriented in-plane. However, the β-phase formation lowers the overall hole conductivity. Therefore, future work will be necessary to isolate α-phase CuPc, in order to be successfully applied into solid-state DSSCs.

4.4 Surface Morphology of TiO_2 Nanoporous Electrode by SEM

The nanoporous structure of TiO_2 electrode is a prerequisite for an efficient DSSC, providing large surface area for dye loading. It is thus important to characterize the surface morphology of our TiO_2 thin film by scanning electron microscopy (SEM). SEM visually reveals the following useful information: the particle size, the pore size and the dispersion and aggregation of the nanoparticles. Figure 30 shows the SEM characterization of TiO_2 nanoporous electrode, which was prepared by screen printing of the TiO_2 paste (see Section 3.1.1). First, it is obvious that our TiO_2 thin film has a porous structure. The pore size is found to be around 25 nm. Second, no apparent aggregation of TiO_2 nanoparticles could be observed. They are randomly distributed on the substrate. Third, some big pores with a diameter of 50 ~ 100 nm have been shown, resulting from the shrinkage of TiO_2 thin film during quick temperature variance in sintering. To conclude, the morphology characterization by SEM confirms the porous property of our screen printed TiO_2 thin film, which is a necessasity for the DSSC fabrication.

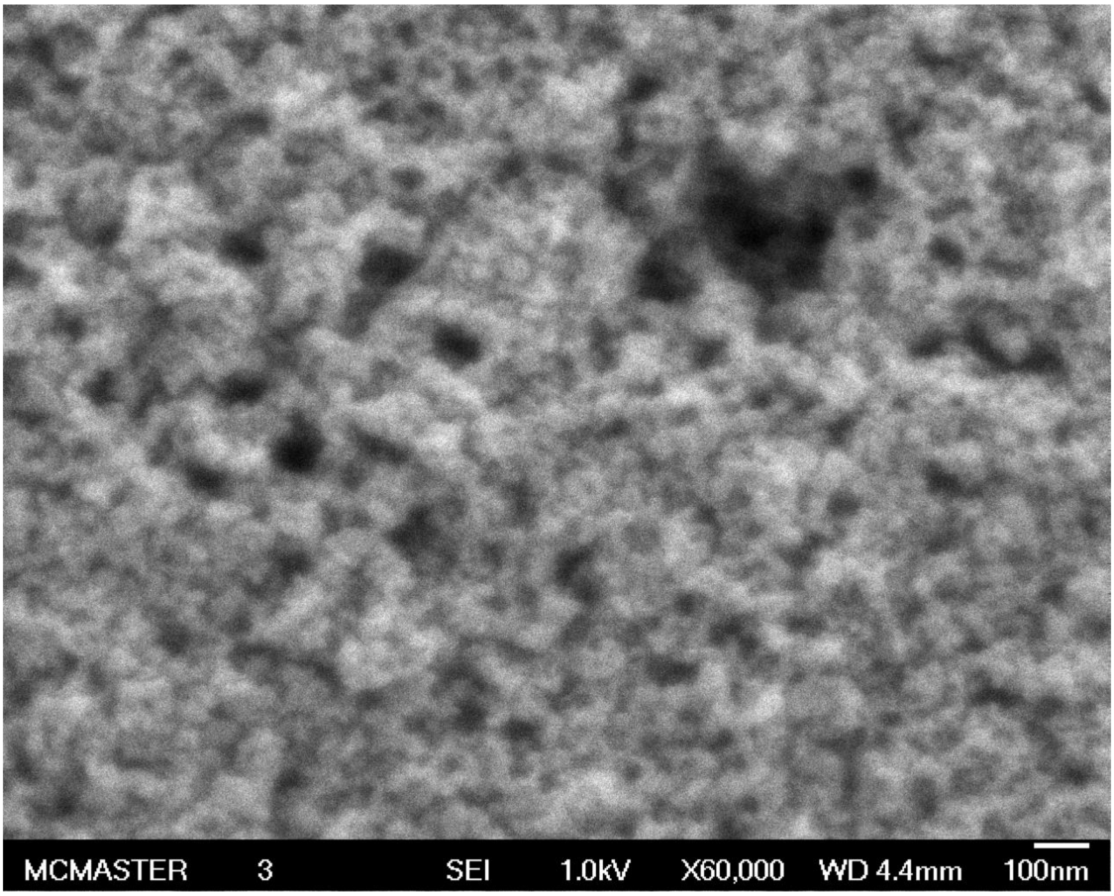

Figure 30: SEM photograph of screen printed nanoporous TiO_2 films showing the surface morphology of TiO_2 with a magnification of 60,000 under 1.0 kV accelerating voltage of electron beam.

4.5 Enhanced TiO_2 Electron Transport by CuPc Doping

To explore the possible role of CuPc in the working electrode, CuPc was doped on the surface of the TiO_2 nanoporous layer, using the procedure described in Section 3.2.2

The device structure is: FTO / TiO_2 compact layer (~20 nm) / TiO_2 nanoporous layer (~12 μm) / CuPc Layer (~1 μm) / N719 dye (~1 nm) / electrolyte (I^-/I_3^- redox couple) (~50 μm) / Pt counter electrode (~10 nm) / FTO, as depicted in Figure 31. It is found that the electron transport in TiO_2 is enhanced after CuPc doping from the comparison of I-V curves obtained from different device structure (see Figure 32).

The I-V curves of CuPc doped and undoped DSSCs are compared in Figure 32. Substantial increase of short-circuit current is observed in CuPc doped cell, from 1.6 mA / cm^2 to 2.4 mA / cm^2. However, the enhanced short-circuit current is accompanied by a slight decrease of open-circuit voltage, from 0.58 V to 0.52 V.

The detailed mechanism of the enhancement of photo current is still under investigation. It is possibly due to the reduced internal recombination rate. CuPc layer acts as an energy barrier in the recombination process between the electrons in TiO_2 and triiodide (I_3^-) in electrolyte.

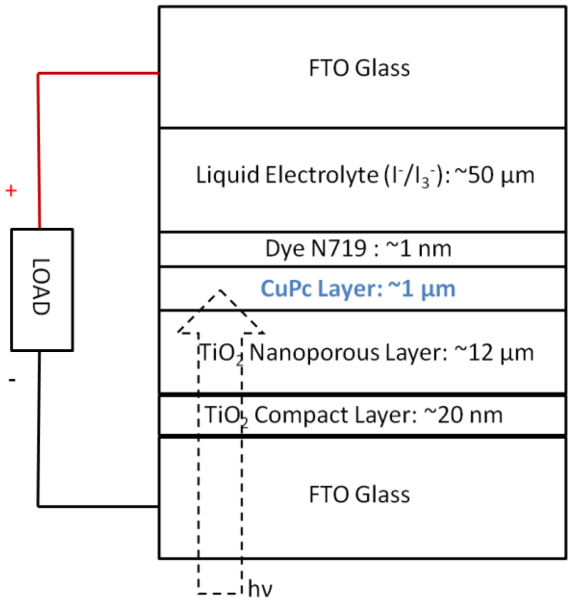

Figure 31: Device structure of CuPc doped DSSC with liquid electrolyte.

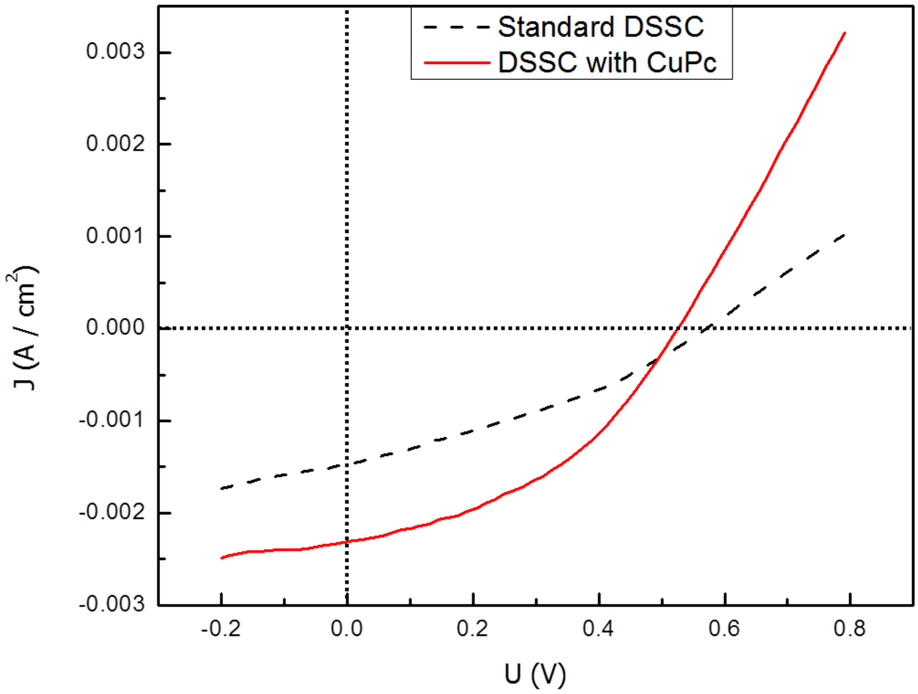

Figure 32: I-V curves of liquid electrolyte involved DSSCs with and without CuPc doping (illumination intensity: 100 mW / cm^2). The solid line is CuPc doped DSSC with electrolyte, while the dash line represents the DSSC.

Chapter 5 Conclusion

In this thesis, the dye-sensitized solar cell (DSSC) with liquid electrolyte is first duplicated and its instability is verified, leading to the need of more stable redox mediators, redox couple or hole conductor. Solid hole conductor copper phthalocyanine (CuPc) is then employed with its intrinsic high thermal and chemical stabilities, to replace the volatile liquid electrolyte in DSSCs. But a lower short circuit current is found in the CuPc solid state device from I-V curve, which is closely related to the inefficient hole transport in the CuPc thin film. Therefore, 2D grazing incidence XRD is utilized to study the phase and texture of CuPc thin film, which helps to explain the lower short-circuit current. It is found that the CuPc thin film has an average crystallite size about 24 nm. In addition, crystallites in the thin film had two preferred orientations $(20\bar{1})$ and (001), with $(20\bar{1})$ dominating. The crystallites in both orientations have a preferential ordering along the substrate normal, and are randomly oriented in-plane. Besides, the film has a cystallinity of greater than 80%, which is good for hole conducting. However, the β-phase formation lowers the overall hole conductivity. The hole conductivity of β-phase CuPc is two-magnitude smaller than that of α-phase CuPc, due to a less overlap in the π-π stacking. As a result, the low hole conductivity of β-phase CuPc is one reason that leads to an inefficient hole transport and reduce the short-circuit current of the solid state DSSC. Therefore, future work will be necessary to isolate α-phase CuPc, in order to be successfully applied into solid-state DSSCs.

Chapter 6 Future Work

Based on what has been accomplished in the dye-sensitized solar cell area, future research into semiconductor metal oxide acetone sensor is also proposed. They both belong to the category of semiconductor metal oxide electronic devices, taking the semiconductor metal oxide nanoparticles advantages including large surface area and the semiconducting properties in the practical operation.

Before we come to the details of the device, a brief introduction to the research and challenge are described in section 6.1.

6.1 Description of Research and Challenge

Noninvasive breath acetone detection plays an important role in diagnosis of diabetes and management of daily insulin injection [79], serving as a rapid and economic alternative to conventional standard blood analysis [80]. Currently, several methods have been employed to trace the exhaled acetone. The most widely used methods involve chromatography with flame ionization detection [81] and selected ion flow tube mass spectrometry [82]. However, the heavy instrument weight, time-consuming sample gases pretreatment and high cost limit their daily utilization by clinics or diabetic patients [80]. Thus, more efforts have been taken to the development of new approaches for portable, low cost breath acetone sensors. Some representatives are fuel-cell based sensors [83] and metal oxide semiconductor sensors [80] [84] [85].

Breath acetone sensor requires high sensitivity (ppb) and selectivity over various gases, for the accurate diagnosis of diabetes. Breath acetone concentration at normal level is between 0.22 - 0.80 ppm, via health metabolism, while for diabetic persons, the content goes beyond 1.80 ppm [86], resulting from metabolizing fat for energy without oxidizing blood glucose [80]. However, it is hard to accurately detect breath acetone, because of its low concentration in the exhalation, and the complicated matrix of breath which includes NO, CO, acetone, ethanol, ammonia and so on [87]. In the detection of breath acetone, breath ethanol has interfered the sensitivity and selectivity the most, since both have similar chemical properties (*e.g.*, molecular structure) and physical properties (*e.g.*, boiling point). The approximate normal breath ethanol concentration (usually associated with fruit consumption) is no more than 0.13 ppm (ca. 0.29 % by volume in blood [88]). Therefore, the challenge of this research is to enhance the selectivity of acetone detection sensor over ethanol. For the fuel cell-based acetone sensors, cross-selectivity of ethanol has been shown [89], due to the larger oxidation energy of acetone compared with ethanol. Additionally, fuel cell sensor lacks stability under dry weather [90], which affects negatively the reliability of the results. Moreover, the requirement of a large amount of noble metal based catalyst increases sharply the cost of the sensor. To solve the latter problem, photocatalyst TiO_2 can be employed into the fuel cell sensor. Excited by the ultra violet light (photon energy >3.2 eV), the electron-hole pair in the TiO_2 will be separated by the built-in electric field at the TiO_2/electrolyte interface, followed by the hole transport to oxidize acetone [91]. Though it can operate at room temperature with a 15W UV lamp, its low sensitivity (acetone concentration ~100 ppm) and low selectivity [92] [93] hinder its detection of breath acetone (0.2 ~ 2 ppm [81] currently. As a result, high selectivity and sensitivity metal oxide semiconductor sensor, as indicated by more recent literature [94], has been chosen to meet the challenge.

6.2 Research Plan

Metal oxide semiconductor (MOS) sensor has the advantages of low cost, easy fabrication, light weight for portability, high sensitivity (0.2 ppm ~ 2 ppm [94]) and less restriction on the testing environment. The challenge here, is to fabricate a metal oxide semiconductor with the ability of sensitivity distinguishing acetone from other gases, especially ethanol, at lowest power consumption (High Temperature Power Source can be lower than 1 watt, which should not be a serious concern for the portable breath acetone detector, according to the literature [80] [95]).

MOS (n-type) sensor is operated by the oxidation of gases in oxygen species adsorbed on a heated surface of MOS. The adsorption of oxygen species on the surface of metal oxide receives electrons from metal oxide, thus increase the resistance. Once reductive gases such acetone arrive on the surface, they will be oxidized by transporting electrons back to the metal oxide surface, thus decreasing the MOS resistance. The high surface area of the metal oxide semiconductor made by nanoparticles benefits the O_2 adsorption, leading to a faster response to acetone.

The methodology has been developed in accordance with references [85] [86] [94]:

1) Sensor preparation: deposit metal oxide semiconductor thin film (TiO_2, ZnO suspension by spin coating or spray coating) on Pt-electrode coated alumina substrate.

2) Connection to a commercial heater.

3) Integrate the sensor with high threshold indicator, comparator, low

threshold indicator, power and power switch.

4) Test the response of the sensor to the blow gases similar to breath, under elevated temperature, to find out the best operation condition for acetone selectivity and sensitivity. Here, the response is described by the ratio of the resistance of sensor in air to the resistance in the target gases [85] [86] .

5) Characterization of the sensor, including surface morphology characterization by optical microscopy, scanning electron microscopy and BET detection of the specific area of the metal oxide semiconductor.

To summarize, non-invasive metal oxide semiconductor based breath acetone detection focuses on monitoring diabetes, a significant long-life health issue. The access to such kind of detector with portability, sensitivity, selectivity and low cost will benefit the diabetic patients in their management of insulin injection. Besides, for the common people in a diet, the device can simultaneously depict their metabolism situation with further calibration. Furthermore, because of its portability, high sensitivity and selectivity, it can be utilized for the environmental detection as well.

(Note: All the power conversion efficiency and short-circuit current data in this thesis were severely lowered by the bad light source used in the experiment, which was later found to be 5 – 6 times weaker than a standard solar simulator.)

Bibliography

[1] C. Hu, "Modern Semiconductor Devices for Integrated Circuits", 1st ed, Berkeley: Pearson, USA, 2010.

[2] T. Ameri, G. Dennler, & C. Lungenschmied *et al*., J. Brabec, *Energy Environ. Sci.* **2**, 347 (2009).

[3] ObservatoryNANO official website, available online: http://www.observatorynano.eu/project/document/2016/. [Accessed 2 March 2012]

[4] K. Wang, "Nanomaterials: from Interfacial Characteristics to Device Applications", Ph.D. Dissertation, McMaster University, ON, Canada (2011).

[5] J. Nelson, *Science* **293**, 1059 (2001).

[6] C. J. Brabec, S. Sariciftci, & J. C. Hummelen, *Adv. Funct. Mater.* **11**, 15 (2001).

[7] J. Li, & A. C. Grimsdale, *Chem. Soc. Rev.* **39**, 2399 (2010).

[8] U. Bach, D. Lupo, & P. Comte *et al.*, *Nature* **395**, 583 (1998).

[9] M. Gratzel, *MRS Bulletin* **30**, 23 (2005).

[10] A. Yella, H. Lee, & H. N. Tsao *et al*., *Science* **334**, 629 (2011).

[11] A. Hagfeldt, G. Boschoo, & L. Sun *et al*., *Chem. Rev.* **110**, 6595 (2010).

[12] M. K. Nazeeruddin, S. M. Zakeeruddin, & R. Humphry-Baker *et al*., *Inorg. Chem.* **38**, 6298 (1999).

[13] M. K. Nazeeruddin, A. Kay, & I. Rodicio *et al*., *J. Am. Chem. Soc.* **115**,

6382 (1993).

[14] T. Daeneke, T. Kwon, & A. B. Holmes *et al.*, *Nature Chem.* **3**, 211 (2011).

[15] Z. Wang, K. Sayama, & H. Sugihara, *J. Phys. Chem. B* **109**, 22449 (2005).

[16] G. Oskam, B. V. Bergeron, & G. J. Meyer *et al.*, *J. Phys. Chem. B* **105**, 6867 (2001).

[17] B. O'Regan, & M. Gratzel, *Nature* **353**, 737 (1991).

[18] C. M. Elliott, *Nature Chem.* **3**, 188 (2011).

[19] D. R. Gaskell, "Introduction to the Thermodynamics of Materials", 4th ed., New York, Taylor & Francis Group (2003).

[20] H. Gerischer, & B. Bunsenges, *Phys. Chem.* **72**, 437 (1968).

[21] B. A. Gregg, "Organic-based ("Excitonic") Solar Cells," National Renewable Energy Laboratory, Golden, CO (2003).

[22] S. A. Haque, E. Palomares, & B. M. Cho *et al.*, *J. Am. Chem. Soc.* **127**, 3456 (2005).

[23] S. Pelet, J. E. Moser, & M. Gratzel, *J. Phys. Chem. B* **104**, 1791 (2000).

[24] J. N. Clifford, E. Palomares, & M. K. Nazeeruddin *et al*., *J. Phys. Chem. C* **111**, 6561 (2007).

[25] H. Hoppe, & N. S. Sariciftci, *J. Master. Res.* **19**, 1924 (2004).

[26] H. Halme, P. Vahermaa, & K. Miettunen *et al.*, *Adv. Mater.* **22**, E210 (2010).

[27] DSSC Solar Cell Battery, available online: http://samsungsdi.com/nextenergy/dssc-solar-cell-battery.jsp. [Accessed 20 February 2012].

[28] DSSC Technology Trend and Market Forecast (2009-2013), available

online:http://www.solarnenergy.com/eng/service/report_show.php?id=597. [Accessed 20 Fabruary 2012]

[29] Sony's Technology, available online: http://www.sony.net/SonyInfo/technology/technology/theme/solar_01.html. [Accessed 20 February 2012].

[30] Sony's Technology, available online: http://www.sony.net/SonyInfo/csr/SonyEnvironment/technology/solar_cells.htm. [Accessed 3 March 2012].

[31] K. Patch, "Solar cell doubles as battery", available online: http://www.trnmag.com/Stories/2004/120104/Solar_cell_doubles_as_battery_120104.html. [Accessed 27 March 2012].

[32] S. Ito, T. N. Murakami, & P. Comte *et al.*, *Thin Solid Films* **516**, 4613 (2008).

[33] A. V. Shah, H. Schade, & M. Vanecek *et al.*, *Prog. Photovolt.* **12**, 113 (2004).

[34] L. Peter, *Phys. Chem. Chem. Phys.* **9**, 2630 (2007).

[35] B. A. Gregg, *Coord. Chem. Rev*. **248**, 1215 (2004).

[36] P. Wang, C. Klein, & H. Shaik *et al.*, *J. Am. Chem. Soc.* **127**, 808 (2005).

[37] A. Mishra, M. K. R. Fischer, & P. Bauerle, *Angew. Chem. Int. Ed.* **48**, 2474 (2009).

[38] S. Feldt, E. A. Gibson, & E. Gabrielsson *et al.*, *J. Am. Chem. Soc* **132**, 16714 (2010).

[39] S. Hattori, Y. Wada, & S. Yanagida *et al.*, *J. Am. Chem. Soc*. **127**, 9648 (2005).

[40] T. Bessho, E. Yoneda, & J. Yum, M. Guglielmi *et al.*, *J. Am. Chem. Soc.*

131, 5930 (2009).

[41] T. W. Hamann, O. K. Farha, & J. T. Hupp, *J. Phys. Chem. C* **112**, 19756 (2008).

[42] A. Hinsch, J. M. Kroon, & R. Kern *et al.*, *Prog. Photovol. Res. Appl.* **9**, 425 (2001).

[43] M. I. Asghar, K. Miettunen, & J. Halme *et al.*, *Energy Environ. Sci.* **3**, 418 (2010).

[44] H. G. Agrell, J. Lindgren, & A. Hagfeldt, *Solar Energy* **75**, 169 (2003).

[45] H. Greijer, J. Lindgren, & A. Hagfeldt, *J. Phys. Chem. B* **105**, 6314 (2001).

[46] H. Rensmo, S. Sodergren, & L. Patthey *et al.*, *Chem. Phys. Lett.* (274), **51** (1997).

[47] H. Lu, T. F. Shen, & S. Huang *et al.*, *Solar Energ. Mater. Solar Cells* **95**, 1624 (2011).

[48] G. K. Mor, K. Shankar, & M. Paulose *et al.*, *Nano Lett.* **6**, 215 (2006).

[49] Y. Diamant, S. G. Chen, & O. Melamed *et al.*, *J. Phys. Chem. B* **107**, 1977 (2003).

[50] R. A. Sayer, S. L. Hodson, & T. S. Fisher, *J. Solar Energy Engin.* **132**, 021007-1 (2010).

[51] M. Gratzel, *J. Potochem. Photobio. C: Photochem. Rev.* **4**, 145 (2003).

[52] P. Wang, S. M. Zakeeruddin, & J. E. Moser *et al.*, *Nat. Mater.* **2**, 402 (2003).

[53] H. Snaith, A. Moule, & C. Klein *et al.*, *Nano Lett.* **7**, 3372 (2007).

[54] J. K. Koh, J. Kim, & B. Kim *et al.*, *Adv. Mater.* **23**, 1641 (2011).

[55] S. Tan, J. Zhai, & B. Xue *et al.*, *Langmuir* **20**, 2934 (2004).

[56] G. Kumara, M. Okuya, & K. Murakami *et al.*, *J. Photochem. Photobiol. A* **164**, 183 (2004).

[57] B. O'Regan, F. Lenzmann, & R. Muis *et al.*, *Chem. Mater.* **14**, 5023 (2002).

[58] D. Chen, Y. Wang, & L. Zhang *et al*., *Growth Design Commun.* **10**, 2057 (2010).

[59] K. Tennakone, G. R. R. A. Kumara, & I. R. M. Kottegoda *et al.*, *Semicond. Sci. Technol.* **12**, 128 (1997).

[60] K. M. Coakley, B. S. Srinivasan, & J. M. Ziebarth *et al.*, *Adv. Funct. Mater.* **15**, 1927 (2005).

[61] G. Bradshawa, & A. J. Hughes, *Thin Solid Films* **33**, L5 (1976).

[62] B. He, "Two-Dimensional X-Ray Diffractions", 1st ed., Hoboken, New Jersy: John Wiley & Sons, Inc., USA (2009).

[63] GADDS: General Area Detector Diffraction System, V4.1.29, Bruker Analytical X-ray Systems Inc., Madison, WI, USA (1999).

[64] S. Schumann, R. Hatton, & T. S. Jones, *J. Phys. Chem. C* **115**, 4916 (2011).

[65] J. Y. Zeng, "Introduction to Quantum Mechanics", 2nd ed., Beijing: Peking University Press, P. R. China (2007).

[66] L. Deng, K. Wang, & C. X. Zhao *et al.*, *Crystals* **1**, 112 (2011).

[67] A. Varotto, C. Nam, & I. Radovpjevic *et al.*, *J. Am. Chem. Soc.* **132**, 2522 (2010).

[68] A. Sánchez- Díaz, R. Pacios, & U. Munecas *et al.*, *Org. Electron.* **12**, 329 (2011).

[69] R. Hiesgen, M. Räbisch, & H. Böttcher *et al.*, *Solar Energ. Mater. Solar*

Cells **61**, 73 (2000).

[70] R. Resel, M. Ottmar, & M. Hanack et al., *J. Mater. Res.* **15**, 934 (2000).

[71] P. Peumans, S. Uchida, & S. Forrest, *Nature* **425**, 158 (2003).

[72] M. Rusu, J. Gasiorowski, & S. Wiesner *et al.*, *Thin Solid Films* **516**, 7160 (2008).

[73] PowderCell, V2.4, Federal Institute for Materials Research, & Testing, Berlin, Germany (2000).

[74] A. Orsa, "11- 0893, *β* - copper Phthalocyanine," Internatio nal Center for Diffraction Data, Newtown Square, PA, USA. Abailable online: www.icdd.com, PCPDFWIM Software V 2.4 (2003). [Accessed 10 March 2011].

[75] B. Hall, D. Zanchet, & D. Ugarte, *Appl. Cryst.* **33**, 1335 (2000).

[76] L. Lozzi, S. Santucci, & S. La Rosa *et al.*, *J. Chem. Phys.* **121**, 1883 (2004).

[77] Mercury V2.4, The Cambridge Crystallographic Data Centre, Cambridge, UK (2011).

[78] K. Wang, McMaster University, Hamilton, ON, Canada. Personal Communication (2011)

[79] W. Q. Cao, & Y. X. Duan, *Crit. Rev. Anal. Chem.* **37**, 3 (2007).

[80] M. Righettoni, & A. Tricoli, *J. Breath Res.* **5**, 037109 (2011).

[81] J. M. Sanchez, & R. D. Sacks, *Anal. Chem.* **75**, 2231 (2003).

[82] D. Smith, P. Spanel, & S. Davies, *J. App. Physiol.* **87**, 1584 (1999).

[83] L. M. Haverhals, "Fuel Cells as Power Sources and Sensors", Ph.D. Dissertation, University of Iowa, Iowa City, IA, USA (2008).

[84] P. Gouma, A. Prasad, & S. Stanacevic, *J. Breath Res.* **5**, 037110 (2011).

[85] Q. Qi, T. Zhang, & L. Liu *et al*., *Sens. Actuators B Chem.* **134**, 166 (2008).

[86] M. Righettoni, A. Tricoli, & S. E. Pratsinis, *Anal. Chem.* **82**, 3581 (2010).

[87] W. Q. Cao, & Y. X. Duan, *Clin. Chem.* **52**, 800 (2006).

[88] Blood alcohol content, available online: http://en.wikipedia.org/wiki/Blood_alcohol_content. [Accessed 6 March 2012].

[89] N. T. Report, "The Likelihood of Acetone Interference in Breath Alcohol Measurement," US Department of Transportation (1985).

[90] S. Slade, S. A. Campbell, & T. R. Ralph *et al.*, *J. Electrochem. Soc.* **149**, A1556 (2002).

[91] A. Mills, & S. L. Hunte, *J. Photochem. Photobiol. A: Chem.* **108**, 1 (1997).

[92] Y. Ku, K. Tseng, & C. Ma, *Inter. J. Chem. Kinet.* **209**, 209 (2008).

[93] J. Yu, Q. Xiang, & M. Zhou, *Appl. Catal. B: Environ*. **90**, 595 (2009).

[94] L. Wang, K. Kalyanasundaram, & M. Stanacevic *et al.*, *Sens. Lett.* **8**, 1 (2010).

[95] S. Kuhhe, M. Graf, & A. Tricoli *et al.*, *J. Micromech. Microeng.* **18**, 035040 (2008).